# Modelling Frontal Low-Level Jets and Associated Extreme Wind Power Ramps over the North Sea

Harish Baki[1], Sukanta Basu[2,3], and George Lavidas[4]

[1]Geosciences and Remote Sensing, Faculty of Civil Engineering and Geosciences, Delft University of Technology, Delft, Netherlands
[2]Atmospheric Sciences Research Center, State University of New York, Albany, the United States
[3]Department of Environmental and Sustainable Engineering, University at Albany, Albany, the United States
[4]Marine Renewable Energies Lab, Offshore Engineering, Hydraulic Engineering Department, Faculty of Civil Engineering and Geosciences, Delft University of Technology, Delft, Netherlands

**Correspondence:** Harish Baki (h.baki@tudelft.nl)

**Abstract.** The increasing global demand for wind power underscores the importance of understanding and characterizing extreme ramp events, which are significant fluctuations in wind power generation over short periods, that pose challenges for grid integration. This study focuses on modeling frontal low-level jets (FLLJs) and associated extreme ramp-down events, particularly their impact on wind power production at Belgium offshore wind farms. Using the Weather Research and Forecasting (WRF) model, we analyzed five cases of extreme wind power ramp down events, including in-depth analysis of two cases and generalization of three additional cases. We assessed the sensitivity of various model configurations, including initial and boundary condition (IC/BC) datasets (ERA5 and CERRA), the activation of Fitch wind farm parameterization (WFP), planetary boundary layer (PBL) schemes, and single versus nested-domain configuration. Our findings indicate that CERRA IC/BCs provide a superior representation of atmospheric flow compared to ERA5, resulting in more accurate predictions of ramp timing, intensity, and FLLJ characteristics. The WFP significantly impacts wind power output by modeling turbine interactions and wake effects, leading to slightly lower wind speeds. The scale-aware Shin and Hong PBL scheme yielded a stronger FLLJ core at higher altitudes with a more pronounced jet nose, although wind speeds below 200 m were lower compared to the Mellor-Yamada-Nakanishi-Niio 2.5 scheme. Single-domain configuration proved more effective in simulating wind power ramps, although higher core heights and higher wind speeds below 200 m, resulting in a diffused jet profile. Our analysis highlights that reliable simulation of extreme ramps associated with FLLJ using a single domain configuration could reduce computational costs. Further, the FLLJ and associated extreme ramps can be predicted one day in advance, offering substantial benefits for operational efficiency in wind energy management.

## 1 Introduction

The demand for global wind power is surging as renewable energy is increasingly seen as essential to combat climate change. The European Union aims for 32% renewable energy by 2030 to reduce greenhouse gas emissions by at least 55% (European Union, 2018). Offshore wind farms (OWFs) are pivotal in meeting these goals, despite their higher construction and mainte-

nance costs compared to onshore wind farms (Zheng et al., 2016). This is due to two main factors: the higher capacity factor of OWFs, as offshore winds are generally 25% stronger and can be utilized 2-3 times longer than onshore winds (Tambke et al., 2005), and technological advancements that allow for the use of larger, more efficient turbines (Mehta et al., 2024). By 2019, Europe's OWF capacity reached 22 GW, with 77% located in the North Sea. The EU plans to expand offshore wind capacity to 450 GW by 2050, with 47% (212 GW) in the North Sea, necessitating an annual consenting rate of 8.8 GW (Wind Europe, 2019). This makes the North Sea a critical area for OWF development.

A major challenge for integrating large-scale wind power into the grid is managing extreme ramp events, which are significant fluctuations in wind power generation over short periods (Ueckerdt et al., 2015; Mararakanye and Bekker, 2019). Without large-scale energy storage, power production must match power consumption, a balance maintained by transmission system operators (TSOs). Often, ramp-up events necessitate wind farm curtailment because surplus electricity cannot be dispatched, leading to profit loss for farm owners. At other times, when wind power output suddenly increases, conventional power generation, such as coal and natural gas, must reduce output, a process known as cycling (Veron et al., 2018). This cycling lowers the capacity credit of conventional generation. In a more complex manner, during ramp-down events, when wind power output suddenly drops, the supply from conventional power generators must increase to meet demand. TSOs often purchase these resources in competitive markets at high rates. In critical situations, load shedding becomes necessary due to minimal power output from wind farms. Wind farm owners then incur additional costs when they fail to meet specific loads and quotas (Valldecabres et al., 2020).

These challenges were evident in the case of Great Britain offshore wind farms on 3rd November 2014 (Drew et al., 2017). During that day, wind power output increased by 1.1 GW in 2 hours and 45 minutes (ramp-up), followed by a 1.2 GW decrease in 1 hour and 50 minutes (ramp-down). Analysis of the meteorological conditions has shown that the ramp-up was caused by a trough that formed behind a large weather front, while the ramp-down was caused by the subsidence of the trough. This unforecasted event caused a market surplus of 570 MWh at 15:30 due to unexpected generation in the Thames Estuary, and a deficit of 820 MWh at 17:00 due to the sudden drop in generation. The imbalance coincided with high demand, leaving fewer available generation units. Expensive short-term operating reserves were deployed, causing a system buy price spike to £183 per MWh, the 16th highest price of the year. This event underscores the importance of a comprehensive understanding of power ramp events and the atmospheric phenomena that contribute to their occurrence.

Ramp-up events are primarily caused by synoptic-scale weather phenomena, such as cyclones (Lacerda et al., 2017; Drew et al., 2018) and cold fronts (Cutler et al., 2007; Linden et al., 2012; Cheng et al., 2013; Haupt et al., 2014; Marjanovic et al., 2014; Pichault et al., 2021; Pereyra-Castro and Caetano, 2022; Arthur et al., 2020; Veron et al., 2018). These events can also be triggered by mesoscale phenomena, such as thunderstorms (Hawbecker et al., 2017; Cheng et al., 2013; Drew et al., 2018; Pichault et al., 2021) and low-level jets (Freedman et al., 2008). Conversely, ramp-down events occur due to a decrease in wind speed, often triggered by the relaxation of cold fronts (Drew et al., 2018; Zhao et al., 2019; Dalton et al., 2019) and the passage of warm fronts (Cheneka et al., 2021). Practically, ramp-down events pose a greater problem than ramp-up events, primarily due to the significant penalties that wind farm owners may incur from short supply. Additionally, ramp-down events can lead to a decrease in system frequency (Ela and Kirby, 2008).

Gallego-Castillo et al. (2015) pointed out the importance of modeling and understanding the causative meteorological phenomena of extreme ramps, which would help improve ramp forecasting frameworks. Our paper focuses on modeling one such weather phenomenon called the frontal low-level jet (FLLJ) associated with cold fronts, which tends to cause extreme wind power ramp-down events, using the Weather Research and Forecasting (WRF) model.

60
Previous studies, such as Freedman et al. (2008) suggested that a gradual, rather than a sharp, decline in wind speed is more common during cold fronts, making up-ramps more frequent than down-ramps. This is evidenced by a large number of studies focused on ramp-up events associated with cold fronts. However, the FLLJ causes an abrupt wind speed drop that triggers an extreme ramp-down event on a time scale of 15 to 60 minutes, which is a unique flow feature we are reporting in

65
the present study. To the best of our knowledge, we are not aware of peer-reviewed journal articles associating FLLJs with extreme wind power ramp-down events. In fact, there has been a study from our group as a non-peer-reviewed master's thesis work (Dreef, 2019), which conducted some very preliminary cases in Scotland. That prompted a detailed investigation that led to this particular work.

Larger, synoptically driven features have longer time scales and are theoretically more straightforward to model and forecast

70
than local-scale phenomena, which usually require fine-scale information about land-surface conditions and turbulent mixing in the atmosphere (Marjanovic et al., 2014). The FLLJ, though being primarily a synoptic-scale phenomenon, also consists of local-scale features along with their intensity and temporal evolution in specific regions. Thus, while synoptic-scale characteristics are expected to be modeled with relative accuracy, the local-scale features exhibit significant sensitivity to model physics parameterizations, domain configuration, and the resolution of the forcing data~~The FLLJ, being a synoptic-scale phenomenon,~~

75
~~is expected to be accurately modeled and forecasted with relative ease. However, atmospheric phenomena occurring within the atmospheric boundary layer (ABL), such as low-level jets, exhibit significant sensitivity to model physics parameterizations, domain configuration, and forcing data~~ (Storm et al., 2009; Nunalee and Basu, 2014; Aird et al., 2021; Tay et al., 2021; Larsén and Fischereit, 2021; Wagner et al., 2019).

As a first step towards better understanding, we investigate the modeling efforts of extreme wind ramp-down events associ-

80
ated with FLLJs, and their impact on wind power production, using the WRF model (Skamarock et al., 2019). In the mesoscale modeling community, it is well known that the forcing data significantly influence the simulation accuracy (Carvalho et al., 2014; de Linaje et al., 2019; Hahmann et al., 2020). Nonetheless, the fifth generation ECMWF atmospheric reanalysis (ERA5) (Hersbach et al., 2020), existing at a $\sim$32 km resolution, has been the favorite forcing data in wind resource modeling (Olauson, 2018; Ramon et al., 2019; Gualtieri, 2022). However, a recent development in meteorological reanalysis is the Copernicus

85
Regional Reanalysis for Europe (CERRA) (Schimanke et al., 2021; Ridal et al., 2024), offering a significantly improved resolution of 5.5 km. Despite the advantages of CERRA, the data have never been used as forcing data in wind resource modeling. Therefore, the present study aims to capitalize on the capabilities of CERRA data as initial and boundary conditions. The improved resolution of CERRA forcing data makes it possible for such modeling with detailed representation of atmospheric processes and less computational resource utilization. In addition, the FLLJ being an ABL phenomenon, the model accuracy

90
will be more sensitive to the use of appropriate planetary boundary layer (PBL) parameterization (Nunalee and Basu, 2014; Gevorgyan, 2018; Vemuri et al., 2022). The WRF model has the capability to parameterize the interaction of wind turbines

with atmospheric flow through a wind farm parameterization (WFP). However, in the absence of wind farm specifications, it is necessary to understand to what extent the WFP contributes to the modeling accuracy.

Keeping these modeling parameters in mind, we aim to determine how well the FLLJ and the associated ramp-down event can be modeled and assess their impact on wind power production at the Belgium offshore wind farm. We also seek to evaluate the sensitivity of ramp characteristics in terms of timing and intensity, as well as the FLLJ characteristics in terms of core strength and height, to the choice of forcing data, PBL schemes, WFP, and domain configuration.

The organization of this paper is as follows. Section 2 briefly discusses the meteorological background of the FLLJ. The methods used here are introduced in section 3, including the data, description of two case studies, a diverse set of WRF model configurations, and the simulation setup. The results will be presented in section 4. The conclusions and the future scope will be presented in section 5. The appendix consists of additional information, including the description of three additional case studies identified for modeling, comparison between ERA5 and CERRA forcing data, and illustration of some additional results.

## 2 Frontal low-level jet: A meteorological perspective

A Low-Level Jet (LLJ) is a local maximum in the vertical wind speed profile, often referred to as a core or sometimes a nose, characterized by a modest (approximately 2-3 $\mathrm{m\ s^{-1}}$ ~~m/s~~) decrease in wind speed above and below the core. LLJs typically occur within the planetary boundary layer (Bonner, 1968; Hallgren et al., 2023). They can be induced by various mechanisms, including inertial oscillation (Blackadar, 1957; Bonner, 1968), diurnal changes related to surface and terrain characteristics, such as coastal jets (Smedman et al., 1993, 1995; Nunalee and Basu, 2014), large-scale baroclinity influenced by sloping terrain (Xing-Sheng et al., 1983; Gerber et al., 1989), and geostrophic adjustment, as seen in barrier jets (Parish and Oolman, 2010; Li and Chen, 1998).

The Frontal Low-Level Jet (FLLJ) shares similarities with the barrier jet mechanism. Observations by Browning and Harrold (1970) first identified the FLLJ while studying air circulation and precipitation growth in cold fronts over the British Isles. They reported strong wind speeds, ranging from 25 to 30 $\mathrm{m\ s^{-1}}$ ~~m/s~~, just ahead of cold frontal surfaces. Subsequent research has confirmed the existence and characteristics of FLLJs (Browning and Pardoe, 1973; Browning, 1974; Browning and Monk, 1982; Browning, 1986; Browning et al., 1998; Orlanski and Ross, 1977; Thorpe and Clough, 1991; Kotroni and Lagouvardos, 1993; Uccellini and Johnson, 1979; Brill et al., 1985; Dudhia, 1993; Chen et al., 1994; Wakimoto and Murphey, 2008; Demirdjian et al., 2020; Tay et al., 2021). The key characteristics of the FLLJ are as follows:

– It is a band of strong winds with velocities ranging from 25 to 30 $\mathrm{m\ s^{-1}}$ ~~m/s~~, typically located within the 900-850 mb pressure level, and forms ahead of a cold frontal surface.

– It is a synoptic-scale phenomenon that extends several hundred kilometers ahead of the frontal surface.

– The jet's acceleration is driven by the isallobaric term, while the Coriolis torque and advective tendency terms influence its propagation along the frontal surface and adjust its alignment relative to the frontal boundary. ~~The jet's acceleration~~

125 ~~is driven by the isallobaric term, with Coriolis torque and advective tendency terms contributing to its propagation perpendicular to the FLLJ.~~

- An important feature of the FLLJ is the abrupt wind speed drop immediately following the jet, which is accompanied by a significant change in wind direction.

The intense wind speed during the FLLJ, combined with the drastic decrease in wind speed that follows, results in extreme ramp-down events.

130 Despite its well-documented characteristics, there is a notable lack of modeling studies focused on the influence of FLLJs and associated extreme ramp-down events on wind power production. While the basic characteristics of FLLJs are known, detailed knowledge regarding their impact on extreme ramps and wind energy production remains sparse in the literature.

## 3 Methods

### 3.1 Data and description of cases

135 During January 2016 to January 2017, the Belgium offshore wind farm cluster (henceforth BOWFC) consisted of three operational projects: the C-Power, Northwind, and Belwind-I (Li et al., 2021), which had a combined capacity of 712MW.The aggregated power production data and day-ahead wind power forecasts from these wind farms are available at a sampling rate of every 15 minutes, which has been quality-controlled by Elia, the transmission system operator of Belgium's high-voltage electricity grid.

140 During the study period, FUGRO deployed two SEAWATCH wind LiDAR buoys at LOT1 (latitude: $51°42.414'$ and longitude:$3°02.0771'$) and LOT2 (latitude: $51°38.778'$ and longitude: $2°57.0846'$) near BOWFC, as part of a metocean measurement campaign for proposed wind farms near the Dutch coast. The LiDARs measure wind speed and direction at 30 m height and from 40 m up to 200 m at 20 m intervals and record the data at a sampling rate of 10 minutes. The two LiDARs have recorded 100% data during the selected weather events, and the data has been quality controlled and released to the public by
145 https:\www.TNO.nl.

As mentioned earlier, wind speed maximum (with a jet core at a height of 900-850 mb pressure) during the FLLJ and drop right after the frontal passage (Browning and Pardoe, 1973) leads to a severe ramp event. Since the lidar observed wind speeds span only up to 200 m altitude, it is impractical to identify jet nose within this altitude. Consequently, we examined the weather maps provided by the United Kingdom Meteorological Office (UKMO), in conjunction with the Belgium offshore wind farm's
150 measured power production, to identify possible cases where extreme ramps in wind farm measured power output coincided with the passage of cold fronts in the weather maps.~~such that the frontal passages coincide with extreme ramps in measured wind power~~. Based on the criteria, five cases are identified, out of which, two are the primary focus, while the additional three cases are used for generalization. A description of the two cases is provided in the following section, while a description of the additional cases is provided in the Appendix.
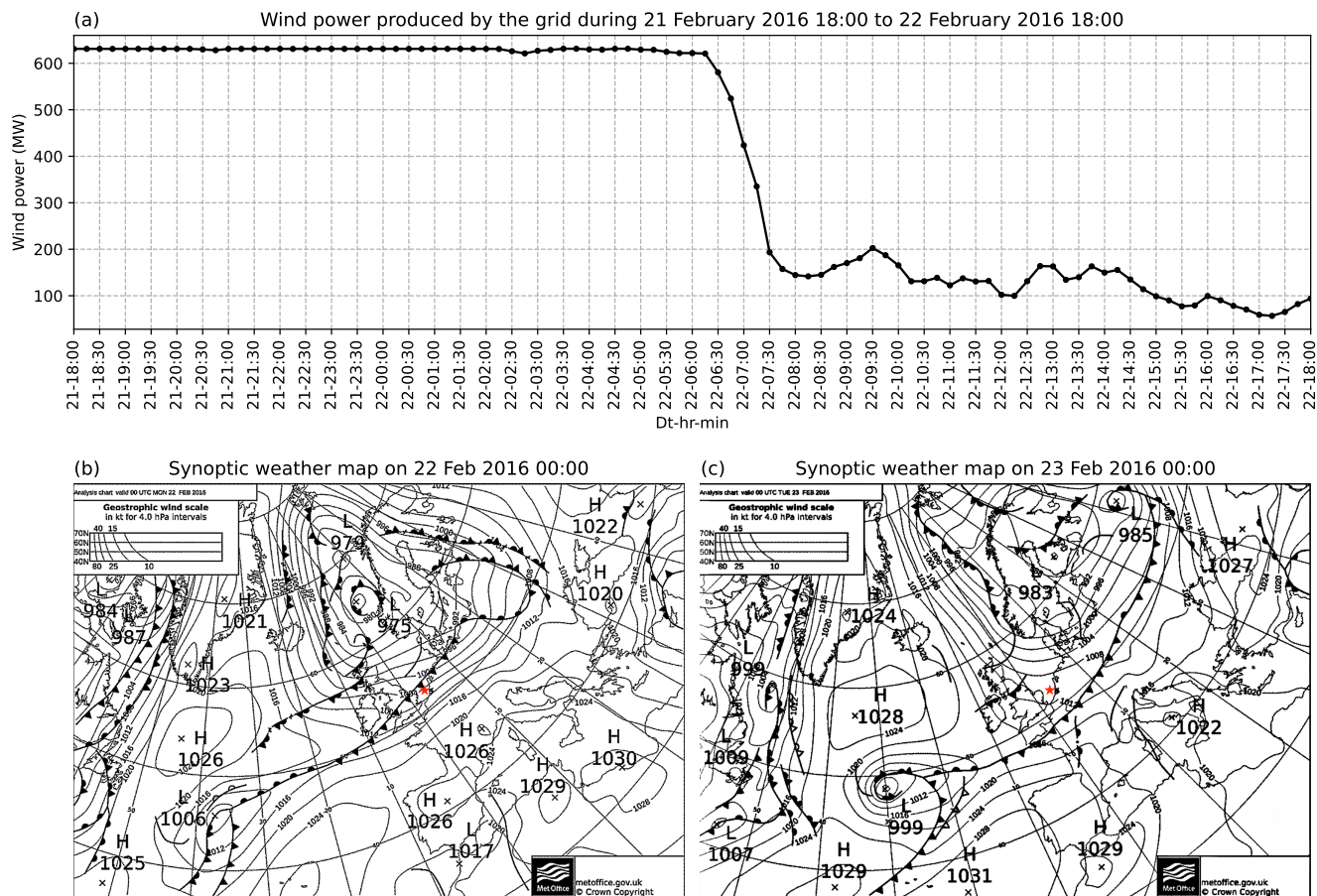
**Figure 1.** (a) The time series of wind power produced by the Belgian offshore wind farms, from 1800 UTC on the 21st to 1800 UTC on the 22nd of February 2016, which depicts the extreme power ramp. The total capacity of the wind farms is 712 MW. Source: https://www.elia.be. (b) Synoptic weather maps on 0000 UTC on 22nd and (c) 23rd February 2016, illustrating a cold front (represented by black line with filled triangles, pointing towards the frontal movement) passing over the Belgium offshore wind farm (illustrated with red star). Source: https://www.wetterzentrale.de/.

### 3.1.1 Case 1

On 22nd February 2016, BOWFC experienced a 54% drop in it's measured wind power within 1 hour, beginning from 0630 UTC, as shown in Fig. 1(a)top panel. The farm is seen producing a maximum wind power of 620 MW, for more than 12 hours period before experiencing the ramp down event, suggesting the occurrence of peak wind speed during this period. Coinciding, the synoptic weather maps at 0000 UTC on 22nd (Fig. 1(b)) and 23rd of February (Fig. 1(c)) clearly illustrating a cold front (dark line with triangles pointing the direction of frontal movement) overpassing the wind farm.
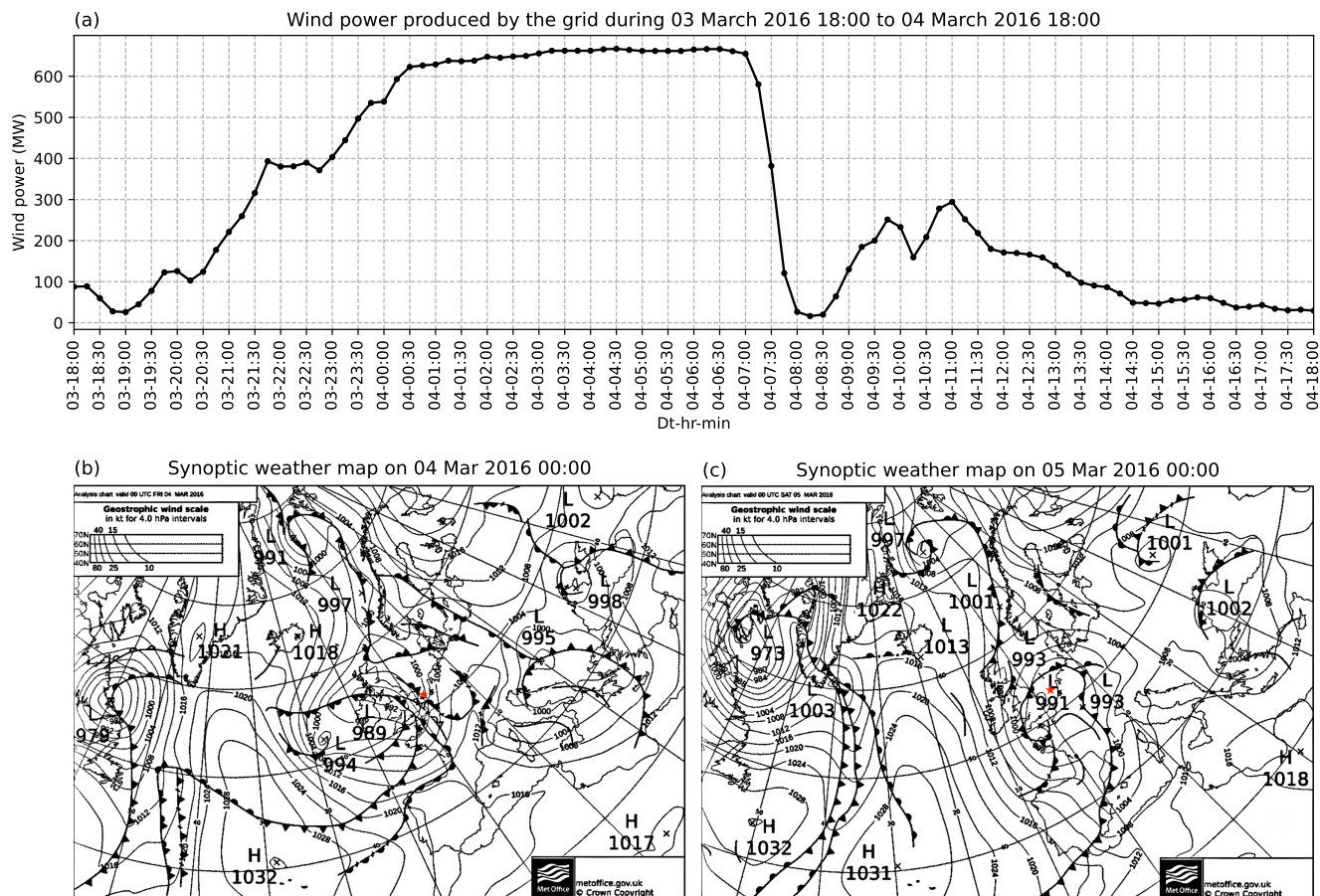
**Figure 2.** Same as Fig. ~~Figure~~ 1, but for case 2. (a) The time series of wind power produced by the Belgian offshore wind farms, from 1800 UTC on the 3rd to 1800 UTC on the 4th of March 2016, which depicts the extreme power ramp. (b) Synoptic weather maps on 0000 UTC of 4th March 2016 and (c) 0000 UTC of 5th March 2016, illustrating a cold front passing over the Belgium offshore wind farm (illustrated with red star).

### 3.1.2 Case 2

Similarly to the above, on March 4th, 2016, BOWFC experienced a 88% drop in its measured wind power within 1 hour, beginning from 0700 UTC, as shown in Fig. 2(a). The farm has been producing power more than 620 MW for four hours before experiencing the severe ramp-down event. The synoptic weather charts at 0000 UTC on 4th (Fig. 2(b)) and 5th of March (Fig. 2(c)) show that a cold front overpassed the wind farm during this period.

**Table 1.** Overview of the WRF model simulations.

| WRF run | IC/BC (frequency) | Grid size, km | Grid points | PBL scheme | Wind farm parameterization |
|---|---|---|---|---|---|
| **ERA5-3d1kmMYFP** | ERA5 (1hr) | 9, 3, 1 | $211 \times 187$, $244 \times 244$, $301 \times 301$ | MYNN 2.5 | on |
| **CERRA-2d1kmMYFP** | CERRA (3hr) | 3, 1 | $181 \times 181$, $301 \times 301$ | MYNN 2.5 | on |
| **CERRA-2d1kmMYnoFP** | CERRA (3hr) | 3, 1 | $181 \times 181$, $301 \times 301$ | MYNN 2.5 | off |
| **CERRA2d1km-SH** | CERRA (3hr) | 3, 1 | $181 \times 181$, $301 \times 301$ | SH | – |
| **CERRA-1d1kmMYFP** | CERRA (3hr) | 1 | $301 \times 301$ | MYNN 2.5 | on |
| **GFS-3d1kmMYFP** | GFS (3hr) | 9, 3, 1 | $211 \times 187$, $244 \times 244$, $301 \times 301$ | MYNN 2.5 | on |

### 3.2 Model configuration

In this study, the WRF model (version 4.4) is utilized to simulate the identified cases. For the sensitivity analysis, we chose to vary the initial and boundary conditions, using ERA5 and CERRA datasets to represent hindcast experiments and GFS (Global Forecasting System) to represent the forecast experiment. Additionally, we varied the domain configuration, planetary boundary layer (PBL) schemes, and activation of wind farm parameterization, in conjunction with the hindcast experiments. In total, five hindcast sensitivity experiments and one forecast experiment were designed, as summarized in Table 1. The innermost domain of all the WRF runs is illustrated in Fig. Figure 3, which is consistently maintained across the runs.

#### 3.2.1 Initial and boundary conditions

We have explored two options for the initial and boundary conditions (IC/BCs), ERA5 and the CERRA, in the hindcast experiments. ERA5 has been released progressively since 2017, and soon after its introduction, it became the preferred reanalysis dataset in the wind power meteorology community. Several studies, like Olauson (2018); Ramon et al. (2019); Gualtieri (2022), and many others, discuss its superior accuracy, lower uncertainty, and higher reliability compared to other global reanalysis
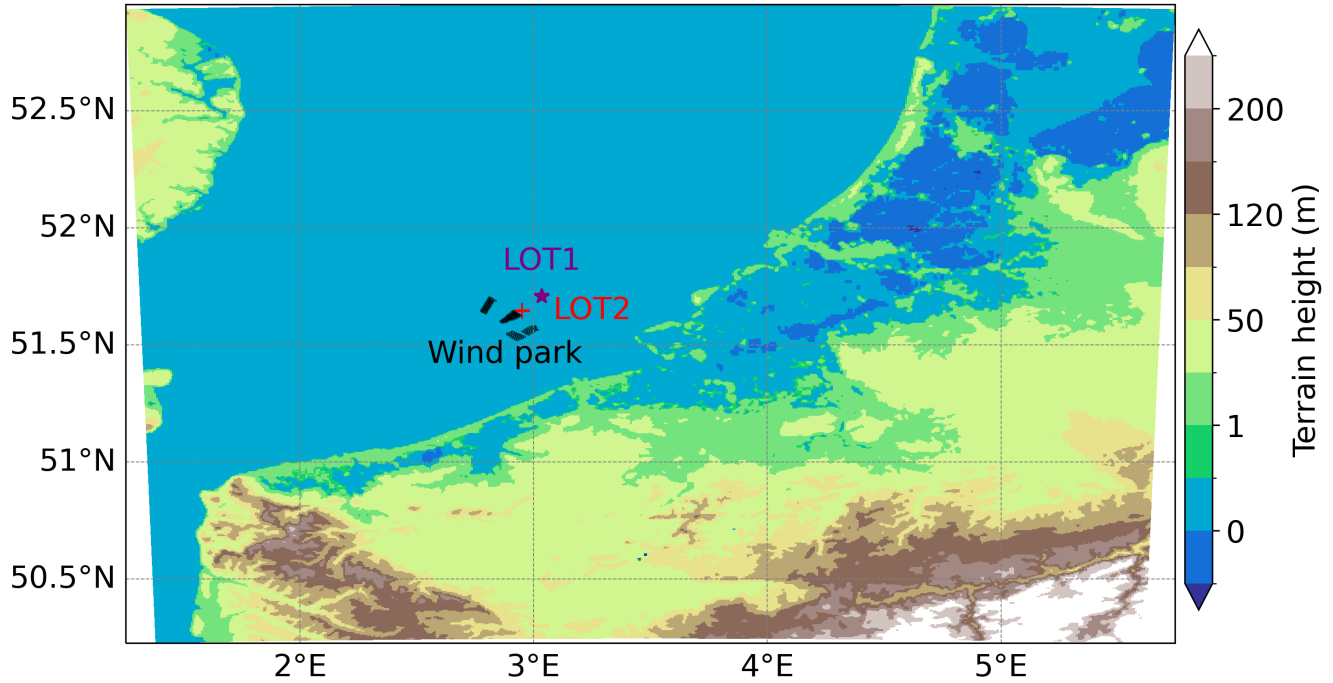
**Figure 3.** A topographical overview of the WRF model simulation domain, encompassing the interested region, consisting of the Belgium offshore wind farm (illustrated with dark filled circles), and two buoy observational locations; LOT1 (illustrated with purple star) and LOT2 (illustrated with red plus). This domain is the innermost domain, that is D03 in ERA5-3d1kmMYFP; D02 in CERRA-2d1kmMYFP, CERRA-2d1kmMYnoFP, and CERRA-2d1kmSH; and D01 in CERRA-1d1kmMYFP simulations.

datasets. The dataset is available at an hourly resolution and a horizontal grid spacing of about 30km. In this study, the ERA5-3d1kmMYFP runs utilize the ERA5 reanalysis at hourly update frequency as forcing data.

180   CERRA provides a high-resolution pan-European reanalysis with a 5.5 km horizontal resolution and 106 vertical levels, covering Europe, Northern Africa, and Southeastern parts of Greenland. The dataset is essentially downscaled from the global ERA5 reanalysis. Unlike the ERA5 data, CERRA provides analysis every three hours. Despite the advantages of CERRA, the data have never been used as driving data for simulations and have not been incorporated into the WRF model configuration. Thus, we aim to capitalize on the fine-scale resolution of CERRA in simulating the extreme ramps associated with the FLLJ

185   events. In doing so, a novel hybrid CERRA-ERA5-based WRF simulation strategy has been developed in this study.

In order to successfully incorporate new forcing data into the WRF model, a new Vtable file needs to be constructed according to the data specifications. After a thorough investigation, it was found that all surface and upper-level meteorological variables needed for the model simulations exist in the CERRA analysis, except soil moisture and soil temperature. Additionally, the WRF model recognizes U and V components of winds, so the 10m wind speed and direction from the CERRA data

190   are transformed into 10m U and V components. A new Vtable corresponding to the CERRA data is created according to the

information provided in the downloaded data files. The CERRA analysis data is ungribbed first using the created Vtable file, while the soil moisture and soil temperature variables from ERA5 reanalysis are ungribbed later using a different Vtable file. After this step, the final metfiles are created, incorporating all the required meteorological variables for the WRF simulations. Except for the ERA5-3d1kmMYFP, the remaining WRF runs utilize the CERRA analysis at a three-hourly update frequency as forcing data.

The sensitivity to driving data in hindcast experiments is assessed through the WRF runs ERA5-3d1kmMYFP and CERRA-2d1kmMYFP. Since ERA5 reanalysis exists at 32 km resolution, we opted for three one-way nested domains for ERA5-3d1kmMYFP runs, consisting of horizontal grid spacing of 9 km, 3 km, and 1 km, in the domains d01, d02, and d03, respectively. On the other hand, the CERRA analysis exists at 5.5 km resolution, thus we chose two one-way nested domains for CERRA-2d1kmMYFP runs, consisting of horizontal grid spacing of 3 km and 1 km, in the domains d01 and d02, respectively.

The initial and boundary conditions provided by reanalysis datasets (e.g., ERA5 and CERRA) tend to be very accurate due to extensive data assimilation. However, in the context of real-time forecasting, such high-fidelity boundary conditions are not available, thus operational forecast data from global models (e.g., GFS) can be used. In the forecast experiment GFS-3d1kmMYFP, cases 1 and 2 are forecasted using a similar configuration as ERA5-3d1kmMYFP, except with GFS real-time forecast data provided as initial and boundary conditions (National Centers for Environmental Prediction, National Weather Service, NOAA, U.S. Department of Commerce, 2015). The GFS IC/BCs during the simulation period are available at a three-hourly resolution and a horizontal grid spacing of about 30km.

### 3.2.2 Wind farm parameterization

The wind farm parameterization (WFP) by Fitch et al. (2012) represents the effects of the wind turbines as a drag-induced energy sink and increased turbulence in the vertical levels containing the rotor disk. The Fitch parameterization assumes that a fraction of the total energy flowing through the wind farm is used for power production (based on the turbine power coefficient), and the rest is converted into turbulent kinetic energy (determined by the turbine thrust coefficient). During the study period, BOWFC consisted of three Belgian offshore wind farms: C-Power, Northwind, and Belwind I, populated with five different types of wind turbines. The wind farms are illustrated as dark filled circles in Fig. Figure 3. More details about each wind turbine, including the power curve, thrust curve, and their corresponding sources, can be found in Li et al. (2021).

The Fitch WFP is well-known for simulating turbine effects, thus it is expected that activating this scheme would result in better wind speed and power simulations. However, the parameterization is only coupled with the MYNN2.5 PBL scheme. To understand the significance of this WFP scheme, we conducted the WRF run CERRA-2d1kmMYnoFP with the WFP turned off, while turned on in the remaining runs with the MYNN2.5 PBL scheme. The sensitivity to Fitch WFP is assessed through the WRF runs CERRA-2d1kmMYFP and CERRA-2d1kmMYnoFP.

### 3.2.3 Planetary boundary layer scheme

Previous studies have emphasized the critical role of PBL schemes in accurately representing wind interactions and turbulence in the lower atmosphere, specifically at the wind turbine hub height (Nunalee and Basu, 2014; Gevorgyan, 2018; Vemuri et al.,

2022). Therefore, we chose two different PBL schemes, namely MYNN2.5 (Mellor and Yamada, 1982; Nakanishi and Niino, 2006, 2009), which has been employed in many wind energy application studies (Jiménez et al., 2015; Jahn et al., 2017; Li et al., 2021), and Shin Hong (SH) scheme (Shin and Hong, 2015), which is a scale-aware scheme, adopted from the studies of Vemuri et al. (2022). The sensitivity to the PBL scheme is assessed through the WRF runs CERRA-2d1kmMYnoFP (without Fitch parameterization) and CERRA-2d1kmSH (inherently no WFP).

The MYNN2.5 and SH PBL schemes differ fundamentally in their approach to turbulence and mixing. MYNN2.5, as a local scheme, relies solely on resolved variables from adjacent grid points to calculate turbulence. In contrast, the SH scheme is nonlocal, using information from multiple vertical levels to determine mixing. It employs scale-aware adjustments and mixing approaches, such as counter-gradient terms or grid-size dependency, to better capture the interplay between the boundary layer and the free atmosphere.

### 3.2.4 Domain configuration

Since the CERRA analysis exists at 5.5 km resolution, which makes it possible to configure the model domain at kilometer resolution without the need for nesting. Thus, to examine the sensitivity to domain configuration, we configured the CERRA-1d1kmMYFP run with a single domain at 1 km resolution. The sensitivity to domain configuration is assessed through the WRF runs CERRA-2d1kmMYFP and CERRA-1d1kmMYFP.

### 3.3 Simulation setup

In this study, the MYNN surface layer scheme (Smirnova et al., 2021) is used in combination with the MYNN2.5 PBL scheme, while the Revised MM5 surface layer scheme (Jiménez et al., 2012) is adopted for the experiments with the Shin-Hong PBL scheme. The remaining physics schemes, including WRF single moment 5-class scheme for microphysics (Hong et al., 2004), RRTMG for shortwave and longwave radiation (Iacono et al., 2008), Unified NOAH for land surface physics (Mukul Tewari et al., 2004), and Kain-Fritsch for cumulus physics (Kain, 2004), are adopted from the studies of Li et al. (2021). The simulations are conducted with a total of 50 vertical levels, spanning from approximately 8 m~~meters~~ above the surface to around 16 km~~kilometers~~ high, with non-uniform grid spacing. The lowest 1 km~~kilometer~~ of the model atmosphere comprises 18 levels. The choice of 50 vertical levels and the corresponding resolution was adopted from Nunalee and Basu (2014).

Event 1 is simulated from 1200 UTC on 21st February 2016 to 1800 UTC on 22nd February 2016, while Event 2 is simulated from 1200 UTC on 3rd March 2016 to 1800 UTC on 4th March 2016. The GFS IC/BCs initialized at 1200 UTC on 21st February 2016 for case 1 and at 1200 UTC on 3rd March 2016 for case 2 are obtained for the forecast experiment. The simulations run for a total of 30 hours, with the initial 6 hours considered as a spin-up period. Output variables, namely wind speed and direction are recorded at 5-minute intervals. If the WFP is activated, the WRF simulation can directly provide wind power production data. For simulations without WFP, wind power production is calculated based on King et al. (2014), which utilizes the turbine power curves and the wind speed at the hub height.

## 3.4 Ramp statistics

In the context of power ramp analysis, we adopt a methodology akin to Drew et al. (2018). A percentage drop in wind power with respect to the rated power is used to capture the intensity and timing of the ramp event, which is computed as,

$$\%\Delta P = \frac{P_{t+\Delta t} - P_t}{P^*} \times 100. \tag{1}$$

Here, $P^*$ is the rated grid power and $P_t$ is the simulated power at time instance $t$. The time scales $\Delta t$ are taken at 15 min, 30 min, and 1 hrs, to quantify the ramp rates.

## 4 Results

### 4.1 Wind power time-series comparison

The time-series data presented in Fig. ~~Figure~~ 4 compares wind power outputs from five WRF simulations to the actual production of the wind farm for two cases. In case 1 (Fig. 4(a)), the wind farm experienced a significant decrease in power output starting at 0630 UTC, while in case 2 (Fig. 4(b)), this decline commenced at 0700 UTC, as detailed in the case descriptions.

During the pre-ramp period (from starting to the ramp occurrence), the wind farm produced a consistent maximum power output, which is attributed to the peak winds associated with the FLLJ. Interestingly, the power output is slightly below the rated capacity of 712 MW. This shortfall is likely due to some turbines being curtailed to prevent damage during high wind speeds or not being in operation. On the other hand, all the WRF model simulations produced power output at the rated capacity, implying that the FLLJ was simulated well. All the simulations produced substantial power drops during the ramp period in both cases, albeit with timing and amplitude discrepancies.

The ramp statistics are computed using Equation 1 and are listed in Table 2 for both cases. In case 1, the wind farm's power output decreased by 19.9% within 15 minutes from 0715 UTC, by 32.3% within 30 minutes from 0700 UTC, and by 54.3% within 1 hour from 0630 UTC. However, the WRF simulations tend to overestimate the intensity of these power drops. Despite overestimating the intensity of the ramp event, the CERRA-1d1kmMYFP simulation well matched the ramp timing. This discrepancy is attributed to the rated power production prior to the onset of the power ramp.

In case 2, the wind farm experienced power drops of 36.7%, 64.6%, and 88.2% within 15, 30, and 60 minutes from 0730 UTC, 0715 UTC, and 0700 UTC, respectively. In contrast to case 1, all the WRF simulations underestimated the ramp intensities across the time scales. Among all, only the CERRA-1d1kmMYFP simulation closely reproduced both the timing and intensity of the power drop, with a 69.5% decrease within 1 hour, matching the observed timing of 0700 UTC.

Comparing the ERA5-3d1kmMYFP and CERRA-2d1kmMYFP simulations, the ERA5 IC/BCs tend to produce ramps at significantly different times, either earlier or later, although their amplitudes are similar to those of the CERRA IC/BCs.

In the comparison between CERRA-2d1kmMYFP and CERRA-2d1kmMYnoFP, the Fitch WFP consistently simulates lower power output than the no-FP run. This discrepancy is attributed to the interaction of wind turbines with the flow and
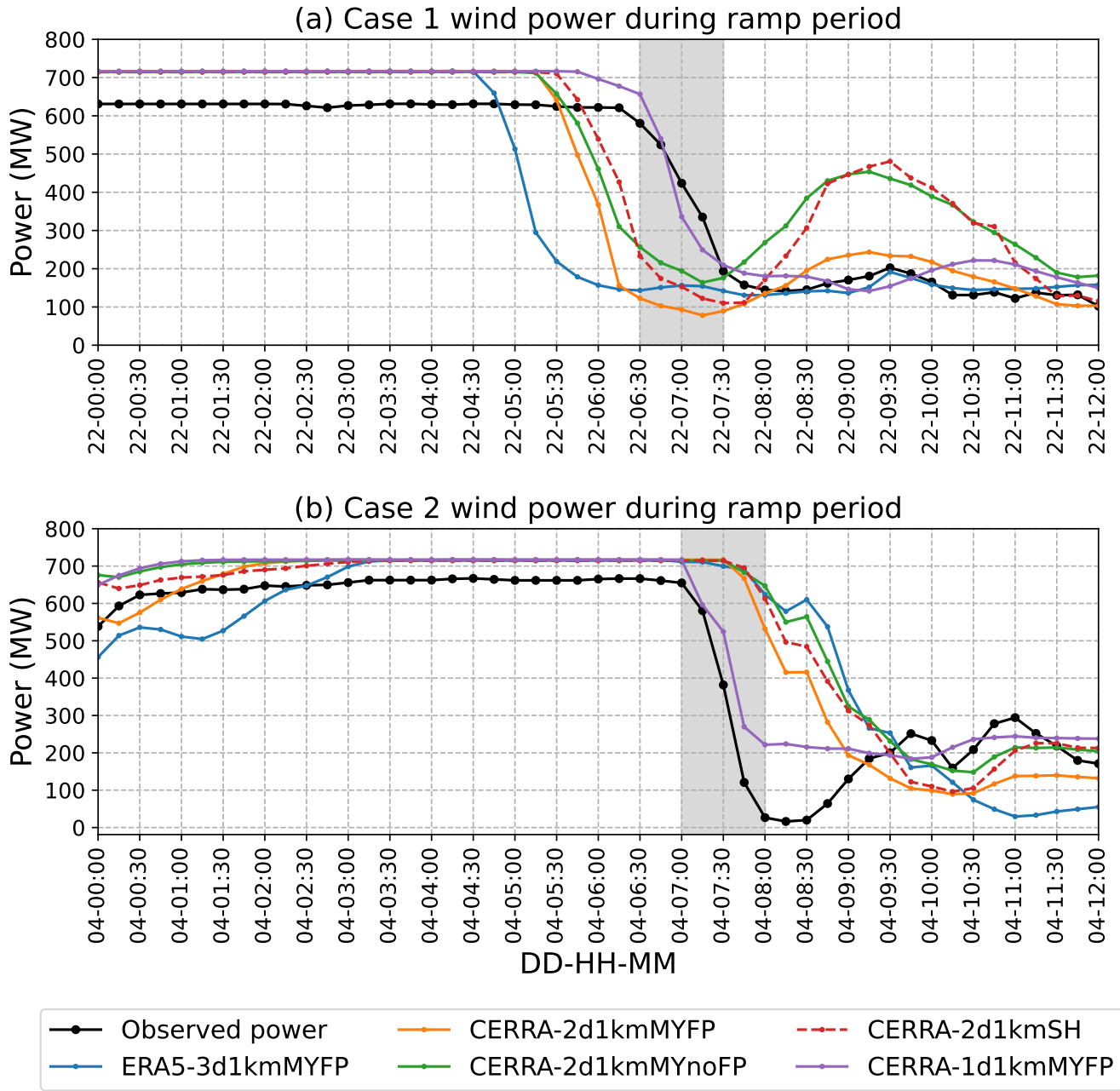
**Figure 4.** A comparison of wind power time series from the five WRF model simulations and the Belgium offshore wind farm production. (a) During 0100 UTC to 1200 UTC on 21st of February, 2016, for case 1. (b) During 0200 UTC to 1300 UTC on 4th of March, 2016, for case 2. The ramp period (1 hour) is shaded in grey.

**Table 2.** Overview of the ramp statistics in wind power in terms of intensity (%) and timing (in parenthesis), at three time-scales: 15, 30, and 60 minutes, obtained from the wind power produced by the Belgium offshore wind farm and the five WRF simulations, during case 1 and case 2. The ramp statistics from measured wind power are presented in bold text.

| Model | Case 1 | | | Case 2 | | |
|---|---|---|---|---|---|---|
| | 15min | 30min | 1hr | 15min | 30min | 1hr |
| **Measured** | **19.9 (07:15)** | **32.3 (07:00)** | **54.3 (06:30)** | **36.7 (07:30)** | **64.6 (07:15)** | **88.2 (07:00)** |
| **ERA5-3d1kmMYFP** | 30.6 (05:00) | 51.2 (04:45) | 69.8 (04:30) | 23.9 (08:45) | 38.1 (08:45) | 52.9 (08:45) |
| **CERRA-2d1kmMYFP** | 29.7 (06:00) | 48.0 (05:45) | 78.4 (05:15) | 19.0 (07:45) | 35.3 (07:45) | 54.1 (07:45) |
| **CERRA-2d1kmMYnoFP** | 21.1 (06:00) | 38.0 (05:45) | 56.4 (05:15) | 16.9 (08:45) | 33.7 (08:30) | 46.8 (08:30) |
| **CERRA-2d1kmSH** | 27.2 (06:15) | 43.0 (06:00) | 67.0 (05:30) | 16.3 (08:00) | 27.9 (07:45) | 42.7 (07:45) |
| **CERRA-1d1kmMYFP** | 28.7 (06:45) | 45.0 (06:30) | 62.8 (06:30) | 35.8 (07:30) | 45.8 (07:15) | 69.5 (07:00) |

the generation of wind wakes. To investigate further, 100 m level wind speed spatial plots from both simulations were examined at various time points for cases 1 and 2, as shown in Figures F1 to F4 in Appendix. The Fitch WFP clearly produced wakes, indicated by a wind speed deficit of 2 $\mathrm{m\,s^{-1}}$ ~~m/s~~ along the wind direction. These wakes extend much farther during FLLJ periods. Due to wake generation, the wind speed simulated by the CERRA-2d1kmMYFP run is slower than in its counterpart. Aside from the vicinity of the wind farm, wind speeds in both runs are almost identical elsewhere.

When comparing CERRA-2d1kmMYnoFP and CERRA-2d1kmSH, the wind power time series are largely similar across cases. The scale-aware SH scheme better captures ramp timing, while the MYNN 2.5 scheme marginally better captures ramp intensity. However, these differences are minimal.

In the comparison between CERRA-2d1kmMYFP and CERRA-1d1kmMYFP, the domain configuration, such as nesting two domains versus a single domain, significantly influences power output. The single-domain configuration in both cases reproduced the power time series more accurately, matching the observed data, unlike its counterpart. Additionally, ramp timing and intensities are better captured by the single-domain setup.

Apart from the aforementioned configurations, we also examined the influence of the number of vertical levels and the choice of spin-up time on simulation accuracy, as discussed in Appendix B and Appendix C. From the analysis, we observed that increasing the number of vertical levels from 50 to 100 moderately deteriorated simulation accuracy. This indicates that higher vertical resolution, while theoretically promising, can introduce complexities that negatively impact model performance under specific conditions. On the other hand, increasing the spin-up time from 6 hours to 12 hours did not result in any significant alterations, suggesting that a 6-hour spin-up period is sufficient for the development of the meteorological features of the weather phenomenon under study.

Overall, there is clear evidence of sensitivity in ramp timing and amplitude with respect to the modeling parameters, with domain configuration and the WFP being the most influential factors.

## 4.2 Wind speed and direction time-series~~serires~~ comparison

The wind speed time-series at different vertical levels from lidar observations at the LOT2 location for cases 1 and 2 are illustrated in Fig. ~~Figure~~ 5 (a-a*). In both cases, a significant drop in wind speed is clearly evident. What distinguishes the two cases is that during the pre-ramp period, there are significant wind speed shears within the 30-200 m layer in case 1, whereas they are only slightly noticeable in case 2. Furthermore, the wind speed drop around 0600 UTC in case 1 is drastic, whereas in case 2, it occurs more gradually from 0600 to 0700 UTC. Nonetheless, in both cases, the wind speed drops at all vertical levels, reaching as low as 6 $\text{m s}^{-1}$~~m/s~~ from as high as 20 $\text{m s}^{-1}$~~m/s~~ in case 1, and 5 $\text{m s}^{-1}$~~m/s~~ from 17 $\text{m s}^{-1}$~~m/s~~ in case 2. Comparing the wind speed time-series with the wind power data, it becomes evident that the ramp timing is one hour ahead in wind speed. This can be explained by the movement of the front and spatial distribution of wind farms, which cannot experience the ramp all at once, whereas lidar observations are measured at a single point.

Similarly, the wind direction time-series from lidar observations at the LOT2 location for cases 1 and 2 are illustrated in Fig. ~~Figure~~ 5 (a-a*). Significant wind directional shifts, approximately $100°$ in case 1 and $130°$ in case 2, are evident in both cases. These shifts align with the wind speed ramp timings, indicating that the wind speed ramp was accompanied by sharp wind directional changes. Unlike the wind speed shears, there are no visible wind veers between the 30-200 m layer, except for occasional fluctuations.

The WRF-simulated wind speed from the five runs is illustrated in Fig. 5(b-f and b*-f*) while direction time-series from five runs are illustrated in Fig. 6 (b-f and b*-f*). Comparing the ERA5-3d1kmMYFP and CERRA-2d1kmMYFP, the simulations forced with CERRA reanalysis were able to reproduce the drastic wind speed drop and wind directional shift in both cases, albeit with considerable timing errors, compared to the observations. Similarly, the simulations forced with ERA5 also reproduced a strong wind speed drop and directional shift in case 1. However, in case 2, the ramp is more gradual, spanning several hours, with a strong directional shift visible three hours later than observed.

The reason for these discrepancies is examined through 100 m wind speed time-series obtained from the original forcing datasets, as shown in Figure D1. ERA5 shows a wind speed drop of 3 $\text{m s}^{-1}$~~m/s~~ in case 1 and 4 $\text{m s}^{-1}$~~m/s~~ in case 2 within one hour, whereas CERRA shows a drop of 9 $\text{m s}^{-1}$~~m/s~~ in case 1 and 4.5 $\text{m s}^{-1}$~~m/s~~ in case 2. From these observations, it is deduced that the coarser representation of the atmosphere in the ERA5 forcing data led to poor dynamical downscaling through the WRF model. In contrast, the better representation in CERRA resulted in more intense wind speed ramp simulations.

Comparing the CERRA-2d1kmMYFP and CERRA-2d1kmMYnoFP, the Fitch WFP simulated winds are 0.5-1 $\text{m s}^{-1}$~~m/s~~ lower than the counterpart. This is due to the generation of wakes by the WFP, which reduces wind speed within the vicinity of the wind farm, as discussed earlier. Apart from the reduced wind speed, the wind speed and directional time-series are identical to one another, with little to no variations.

Comparing the CERRA-2d1kmMYnoFP and CERRA-2d1kmSH, the wind speed and directional time series show some degree of similarity during the pre-ramp and ramp periods. However, the scale-aware SH scheme simulated winds across the cases are consistently lower than the counterpart and also closely align with the observations. In addition, the wind speed ramp in case 2 is abrupt from the MYNN 2.5 scheme, while the SH scheme simulated an initial sharp ramp followed by a gradual

340 reduction in winds to 5 m s⁻¹ ~~m/s~~. These discrepancies suggest that the PBL scheme has some degree of influence on the wind speed and direction simulation.

Comparing the CERRA-2d1kmMYFP and CERRA-1d1kmMYFP, the wind speed and direction produced by the single domain configuration are consistently lower than those from the nested domain configuration. In fact, the wind speed time series during the pre-ramp period from the single domain configuration are very close to the observed ones, with an intermittent

345 wind speed drop in case 1 and a gradual rise in wind speed during case 2. The CERRA-1d1kmMYFP simulation is particularly interesting, as it perfectly captured the ramp timing in both cases. However, in case 1, it reproduced a secondary gradual down-ramp, which is not seen in the observations, nor produced by the nested domain configuration.

Since downscaling is largely governed by the forcing data, the nested domain configuration simulations will considerably modify the initial and boundary conditions (IC/BCs) due to telescopic refining, while the single-domain simulations remain

350 closer to the original IC/BCs. Thus, the better accuracy observed in the single-domain configuration simulation is attributed to the more accurately resolved atmospheric features present in the CERRA IC/BCs.

## 4.3 Wind profiles

To identify the FLLJ and its characteristics in terms of core strength and height, we need wind speed profiles spanning the entire boundary layer. Unfortunately, lidar observations only measure wind speed up to 200 m, which is inadequate for characterizing

355 FLLJs. As an alternative, we utilized the WRF-simulated wind profiles from five runs for the analysis. Knowing that the jet occurs during the pre-ramp period, we extracted the hourly averaged wind speed profiles during different time instances at the LOT2 location, illustrated in Fig. ~~Figure~~ 7 for both cases. Apart from the wind speed profiles, the time-height cross-sections of wind speed at the LOT2 location are also illustrated in Figure E1.

Although there is no universally accepted definition of an LLJ, in this study, we used the definition from Hallgren et al.

360 (2023): an increase in horizontal wind speed of at least 1 m s⁻¹ ~~m/s~~ and 10% of the core speed below the jet core (jet nose) and simultaneously a decrease of 1 m s⁻¹ ~~m/s~~ and 10% above the core. The LLJ core height is marked with a black solid line in Figure E1.

Comparing the ERA5-3d1kmMYFP and CERRA-2d1kmMYFP, in case 1, the ERA5 IC/BCs produced diffused wind profiles at all times, with no defined jet nose identified. On the other hand, the CERRA IC/BCs produced a strong FLLJ core at

365 400 m altitude. In case 2, both IC/BCs produced a defined jet nose, with the CERRA-forced profiles being more diffuse than the ERA5-forced profiles. This suggests that the vertical profiles from the WRF runs are greatly influenced by the forcing data.

To clarify the source of this discrepancy, we investigated the wind speed profiles from the forcing data (metfiles of ERA5 and CERRA simulations' parent domain), as shown in Figure D2, during 0500 UTC for case 1 and 0600 UTC for case 2. Interestingly, the ERA5 forcing data in case 1 resembles an LLJ profile, with a core height at 700 m. However, the ERA5-

370 3d1kmMYFP run failed to reproduce this LLJ profile. Conversely, the CERRA forcing data in case 2 does not resemble an LLJ profile, but the CERRA-2d1kmMYFP run was able to produce an LLJ profile.

Comparing the CERRA-2d1kmMYFP and CERRA-2d1kmMYnoFP, the WFP does not seem to have any significant influence on the vertical wind speed profiles, except for the occasional lower jet core height, which can be attributed to the reduced
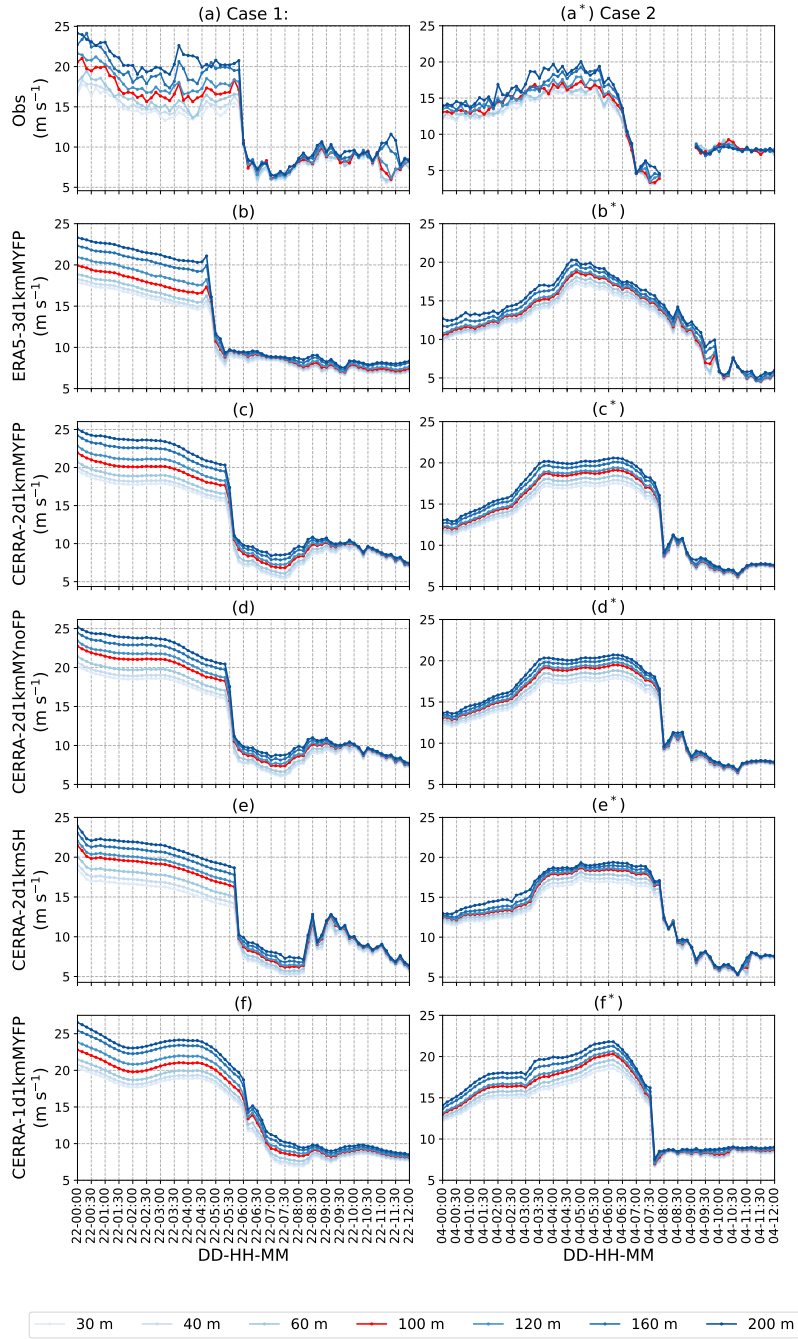
**Figure 5.** A comparison of wind speed time series at seven vertical levels from lidar observations at LOT2 (a-a*) and the five WRF model simulations (b-f and b*-f*). (b-f): during 0100 UTC to 1200 UTC on 21st of February, 2016, for case 1. (b*-f*): during 0200 UTC to 1300 UTC on 4th of March, 2016, for case 2.
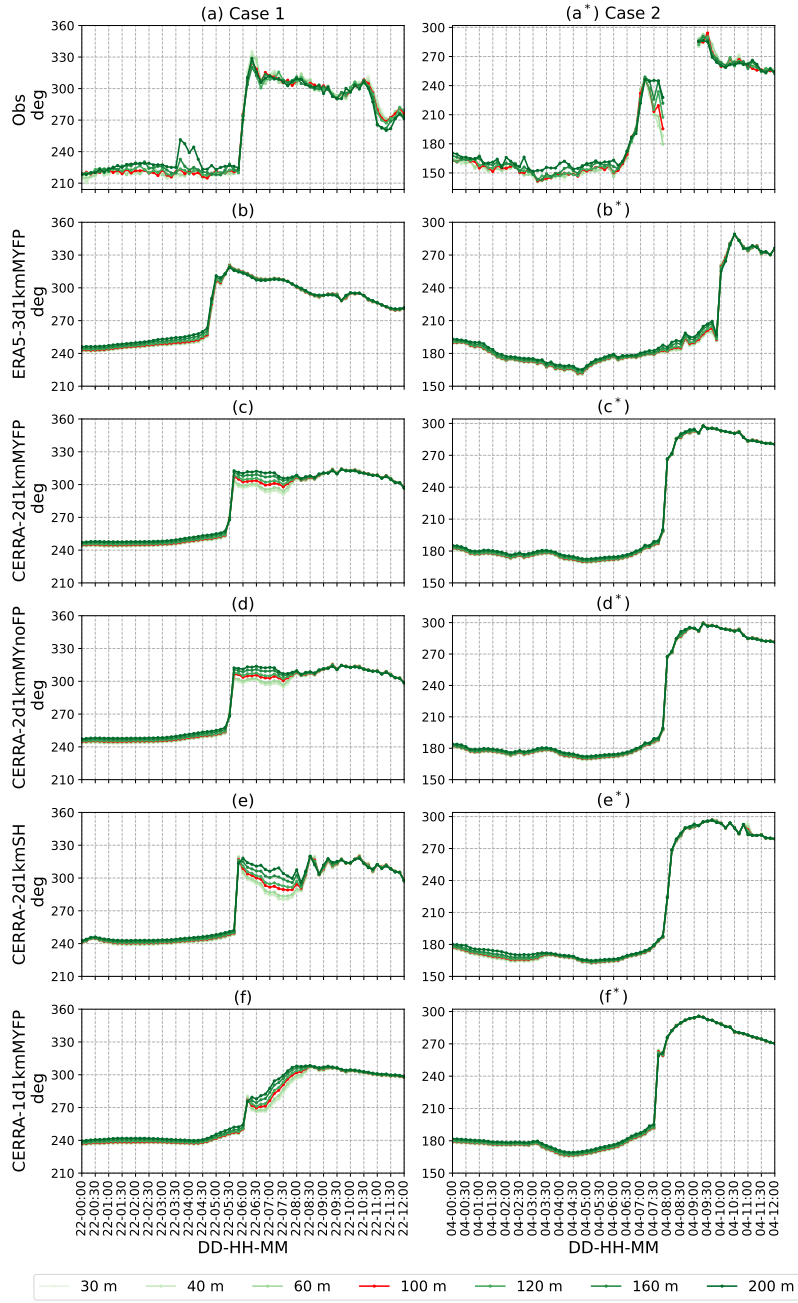
**Figure 6.** A comparison of wind directiion time series at seven vertical levels from lidar observations at LOT2 (a-a*) and the five WRF model simulations (b-f and b*-f*). (b-f): during 0100 UTC to 1200 UTC on 21st of February, 2016, for case 1. (b*-f*): during 0200 UTC to 1300 UTC on 4th of March, 2016, for case 2.

wind speed. Comparing the CERRA-2d1kmMYnoFP and CERRA-2d1kmSH, the scale-aware SH scheme results in a stronger
375 FLLJ core at a higher altitude compared to the MYNN 2.5 scheme across the cases. Additionally, the FLLJ nose is more
defined and pronounced in the scale-aware PBL scheme, suggesting a more accurate representation of the jet characteristics.

Comparing the CERRA-2d1kmMYFP and CERRA-1d1kmMYFP, the single domain configuration notably produced double
peaks in case 1, which seem to stem from the forcing data (as observed in the CERRA profiles from Figure D2), indicating
that the downscaling is largely governed by the forcing data here. In both cases, the single domain configuration produced jet
380 cores at higher altitudes with higher magnitudes than the double nested domain configuration.

Overall, all simulations were able to produce some degree of jet core, but with varying heights and strengths. Interestingly,
the wind profiles are different across the cases, signifying the diversity in characteristics of the two case studies. Since the
profiles are derived from simulations, it is difficult to determine which one is the most accurate. However, it is clear that an
FLLJ exists in both cases, with a wind speed maximum (core strength) of 25 m s$^{-1}$m/s. A clear jet core is located around 700
385 m in case 2, but there is ambiguity in case 1, where the jet core could be around 400 m or 800 m. The differences in the vertical
wind speed profiles across the simulations suggest that while FLLJs are a common feature, their precise characteristics can
vary significantly depending on the model configuration and resolution.

## 4.4 Synoptic characteristics of FLLJ and the associated ramp

To examine the modeling capability of the WRF model in simulating FLLJ and understanding their synoptic characteristics,
390 we conducted surface and cross-sectional analyses of wind speed. The analysis was performed at the wind speed ramp time
instance over the observational site LOT2. From the wind speed time-series shown in Fig. Figure 5, it is evident that the WRF
runs produced wind speed ramps at different time instances. Thus, to eliminate any influence of temporal shift on the FLLJ
synoptic characteristics, we chose wind speed from each WRF run at the corresponding ramp instance, instead of the lidar
observed ramp instance.

395 Accordingly, 200 m level wind barbs from the five WRF runs are presented in Fig. Figure 8 (a-e) for case 1 and Fig. Figure
9 (a-e) for case 2. From all the runs, the wind barbs reveal two distinct systematic wind patterns separated by sharp shifts in
wind direction. This separation represents the boundary between warm and cold air masses, referred to as the surface cold front
(SCF) by Browning and Pardoe (1973). From the WRF runs, the SCF is nearly parallel to the Belgium coast in case 1, while
aligning with the 3° longitude in case 2 (except for the ERA5-3d1kmMYFP, in which the SCF seems to be curved).
400 Winds ahead of the frontal boundary, almost parallel to the SCF, are much stronger than the winds trailing the SCF. From the
studies of Browning and Pardoe (1973), such strong winds ahead and parallel to the SCF are indicative of an FLLJ. Conversely,
the winds trailing the front, expected to be normal to the SCF, display a slight inclination towards the front in case 1, while
remaining perfectly normal in case 2.

Differences in wind speed magnitudes across the WRF runs highlight the influence of modeling parameters. However, the
405 orientation and extent of the FLLJ are consistent across runs, except for ERA5-3d1kmMYFP in case 2. Wind speeds from
ERA5-forced runs are generally lower than those from CERRA-forced runs. The WFP has minimal impact on wind speed
magnitude. When comparing CERRA-2d1kmMYnoFP with CERRA-2d1kmSH, the scale-aware SH scheme results in lower
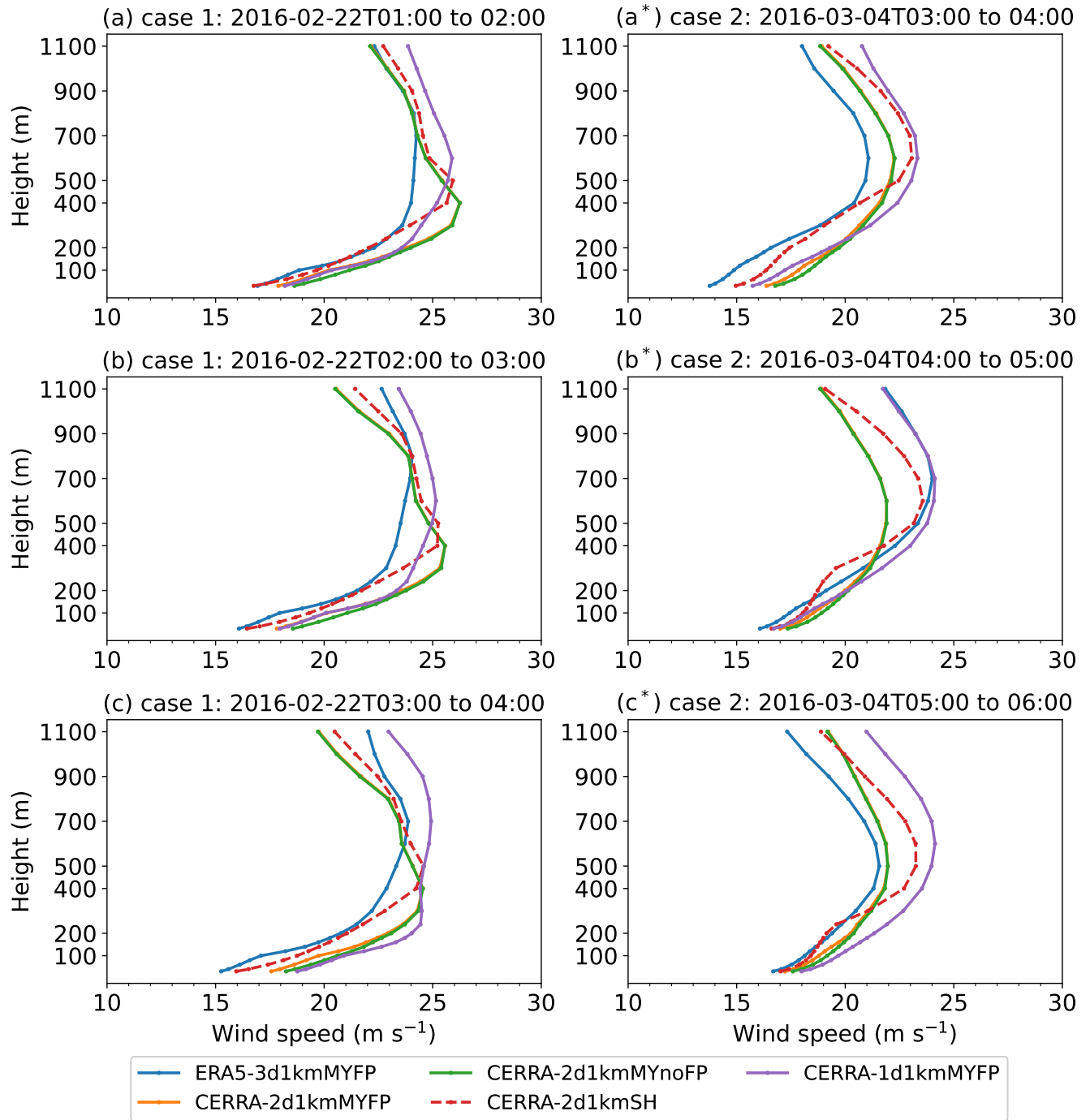
**Figure 7.** Evolution of wind speed profiles from the five WRF simulations, for case 1 (a-c) and case 2 (a\*-c\*), at LOT2 location. The profiles are averaged over an hour during 03:00 to 04:00 (a-a\*), 04:00 to 05:00 (b-b\*), and 05:00 to 06:00 (c-c\*).

FLLJ wind speeds than the MYNN 2.5 scheme. Additionally, in comparing CERRA-2d1kmMYFP with CERRA-1d1kmMYFP, the single domain configuration produces consistently lower wind speeds than the nested domain configuration. Furthermore,

410  the SCF is more distinct in the nested domain configuration compared to the single domain configuration.

To gain further insights, a transect line AB (shown in red) was drawn perpendicular to the frontal surface, equivalent to dissecting the frontal cross-section, which serves as a reference for wind speed cross-sectional analysis. The transect normal velocity component is equivalent to the front-parallel velocity component, shown in 8(a*-e*) for case 1 and 9(a*-e*) for case 2. The abscissa measures distances (km) along the transect line AB to/from the LOT2 location.

415  In both cases, regardless of the modeling parameters chosen, a clear and significant wind speed gradient is visible at the LOT2 location (0 km), indicating the presence of the SCF. Ahead of the SCF, from a distance of 10 km, there is a layer of wind speed maxima (jet core) in the vertical direction, indicative of an FLLJ. The choice of IC/BCs, PBL, and domain configuration appears to influence the FLLJ core strength and height.

In case 1, the ERA5 IC/BCs produced a weak core between 300-500 m altitude, while in case 2, no distinct core was formed.

420  In contrast, the CERRA IC/BCs generated a clear jet core in both cases. For case 1, the core height is 400-500 m within 50 km of the SCF, with a core strength of 22-23 $m\ s^{-1}$m/s. Beyond this range, orographic interactions cause the jet core to rise, reaching 25 $m\ s^{-1}$m/s at about 100 km distance. In case 2, the core is at 400-600 m with a strength of 21 $m\ s^{-1}$m/s, and similarly rises to higher altitudes, reaching 22 $m\ s^{-1}$m/s at approximately 150 km due to orographic interactions.

Comparing CERRA-2d1kmMYnoFP and CERRA-2d1kmSH, the scale-aware SH scheme simulated a higher FLLJ core

425  height in both cases. The core strength is lower in case 1 and higher in case 2 compared to MYNN 2.5 scheme simulations. Additionally, wind speeds below 200 m are consistently lower in the SH scheme.

For CERRA-2d1kmMYFP versus CERRA-1d1kmMYFP, the single-domain configuration resulted in a higher core height and higher wind speeds below 200 m, producing a more diffused jet nose profile across both cases.

From the cross-sectional analysis, it is clear that the front-parallel component mainly contributes to the occurrence of FLLJ,

430  which is in line with the findings of Browning and Pardoe (1973). On the other hand, the front-parallel winds behind the frontal boundary maintain a magnitude of 8-12 $m\ s^{-1}$m/s in case 1, contributing to the observed directional inclination seen in the wind barbs, whereas a magnitude of 0 $m\ s^{-1}$m/s is seen in case 2, as evident from the wind barbs.

The transect-parallel velocity component is equivalent to front-normal velocity component, shown in 8(a$^+$-e$^+$) for case 1 and 9(a$^+$-e$^+$) for case 2. Interestingly, velocity ahead and behind the frontal surface are in the opposite direction and are

435  exactly wedged by the frontal boundary. Findings of Browning and Harrold (1970) confirm that the parallel component behind the front aligns with the frontal surface's movement, while the component ahead of the front directs towards the frontal surface (which actually ascends to the upper levels, not displayed in these figures), a behavior aptly captured by all the simulations.

In both cases, the front-normal velocity ahead of the boundary is much stronger than the velocity behind the boundary. These have two diverse effects: one, winds ahead of the boundary contribute to strengthening FLLJ intensity, and two, winds behind

440  the boundary result in a drastic wind speed drop, ultimately leading to a severe ramp event.

To put together the significance of front-parallel and normal circulations on wind power production, consider any event. An approaching cold front brings FLLJ along with it, spanning hundreds of kilometers ahead of the frontal surface and resulting

in maximized wind power production for several hours. Within the vicinity of the frontal surface, the front-normal component also contributes to further intensifying the FLLJ. Once the front overpasses a wind farm, wind speed drops from an intense 445 FLLJ magnitude to the magnitude of winds trailing the front, resulting in an intense ramp event.

## 4.5 Real-time forecasting

In this section, we investigate whether extreme ramp events associated with FLLJ could have been predicted in a real-time forecast scenario, through the GFS-3d1kmMYFP run. The model forecasted wind power is compared with the grid-measured and Elia day-ahead forecasted power for cases 1 and 2, as shown in Fig. ~~Figure~~ 10. We note that the WRF model was able 450 to forecast the extreme ramp event in both cases, though with some degree of timing mismatch.~~Surprisingly, the WRF model~~ ~~was able to forecast the extreme ramp event in both cases, albeit with some degree of timing mismatch.~~ In contrast, the Elia forecast shows a gradual ramp-down event in case 1, while no ramp was observed in case 2. Additionally, the model accurately forecasted the pre-ramp wind power maxima, implying that the FLLJs are being well forecasted in both cases.

The ramp statistics are computed at a 1-hour time scale and are presented in Table 3. In case 1, the model forecasted the 455 ramp 1 hour and 15 minutes in advance with an overestimation in intensity, whereas the Elia forecast delayed the ramp by 1 hour and 15 minutes with an underestimation in intensity. In case 2, the model forecasted ramp was delayed by 45 minutes with an underestimation in intensity, whereas no such ramp has been detected in the Elia forecasted power (a 17% change in 1 hour is not typically considered a ramp).

To compare, the ramp intensity from the model forecasts is of a similar magnitude to that of the CERRA-2d1kmMYFP 460 simulation for case 1 and to that of the CERRA-1d1kmMYFP for case 2. This implies that extreme ramps can be forecasted well one day in advance, with an accuracy comparable to that of reanalysis dataset simulations.

**Table 3.** Overview of the ramp in wind power in terms of intensity (%) and timing (in parenthesis), at 1 hr time-scale, obtained from the Belgium offshore wind farm inhourse day-ahead forecast and the GFS-3d1kmMYFP simulation, for cases 1 and 2.

| Model | Case 1 | Case 2 |
|---|---|---|
| **Grid-measured** | **54.3 (06:30)** | **88.2 (07:00)** |
| **Elia-forecast** | 33.2 (07:45) | 17.7 (10:00) |
| **GFS-3d1kmMYFP** | 73.1 (05:15) | 64.2 (07:45) |

## 4.6 Generalization across multiple cases

So far, the results have been focused on the analysis of two cases. To generalize the robustness of the WRF model in simulating the extreme ramp events associated with FLLJ, three more cases have been simulated using configurations with CERRA 465 IC/BCs. The synoptic charts and the measured wind power time-series of these additional cases are illustrated in Figures A1 to A3, showcasing extreme ramp events. Case 3 is simulated from 1800 UTC on the 8th to 0000 UTC on the 10th of February 2016, case 4 is simulated from 0600 UTC on the 9th to 1200 UTC on the 10th of January 2017, and case 5 is simulated
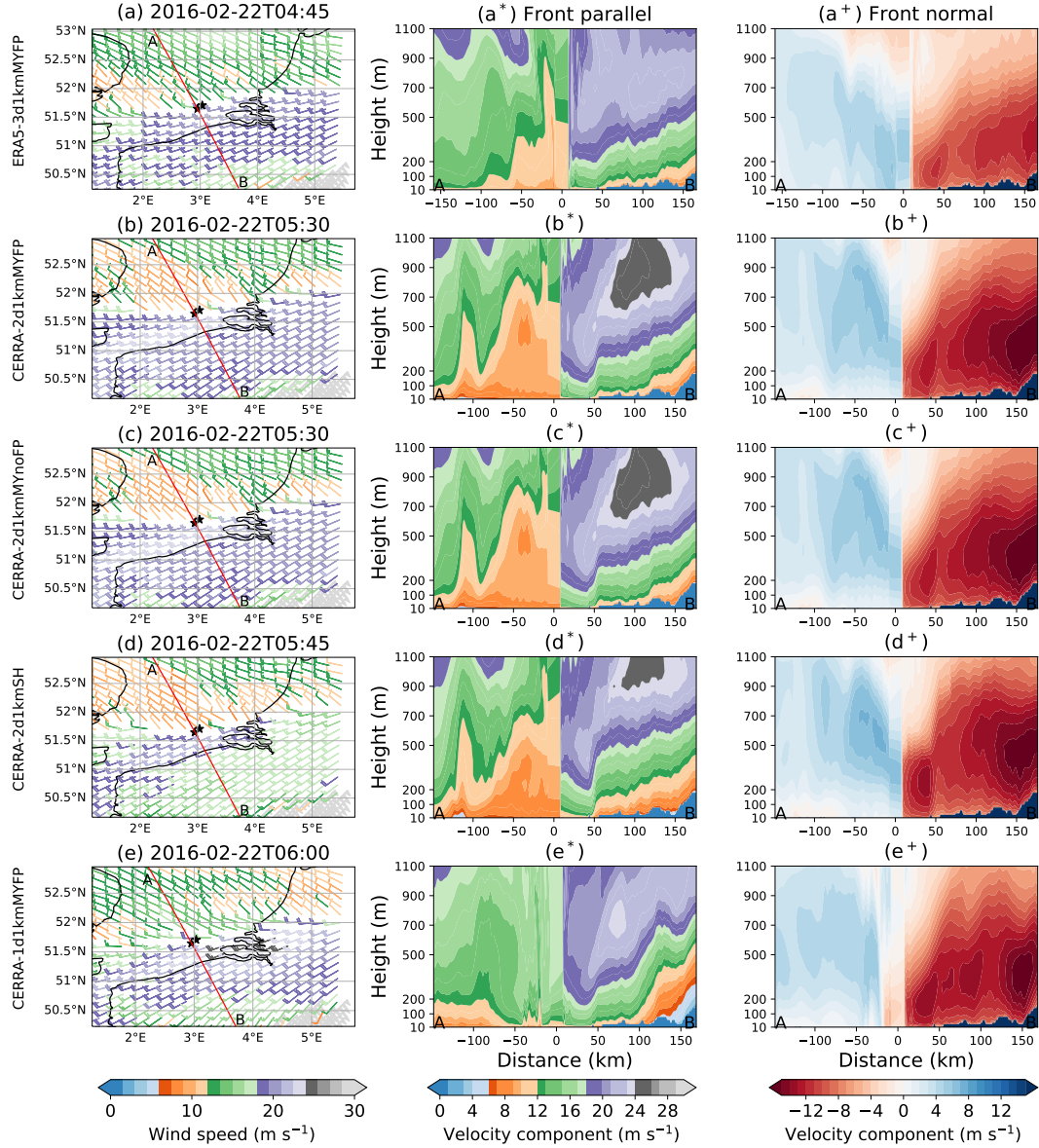
**Figure 8.** Illustration of horizontal wind speed from the five WRF runs: ERA5-3d1kmMYFP (a-a+), CERRA-2d1kmMYFP (b-b+), CERRA-2d1kmMYnoFP (c-c+), CERRA-2d1kmSH (d-d+), and CERRA-1d1kmMYFP (e-e+), for case 1, during ramp time instances of the corresponding WRF run. (a-e): spatial distribution of wind barbs at 200 m level. The ramp instances of the corresponding WRF run are listed as center title. A transect line AB in red color is drawn perpendicular to the frontal surface, while the buoy locations LOT1 and lOT2 are illustrated with black stars. (a*-e*): The velocity component is normal to the transect line AB, which gives an idea about the front parallel wind speed. (a+-e+): The velocity component is parallel to the transect line AB, which gives an idea of the front's normal wind speed. The abscissa in the middle and bottom panels is the distance (km) along the transect line AB to/from the LOT2 location, whereas the ordinate is vertical level (m).
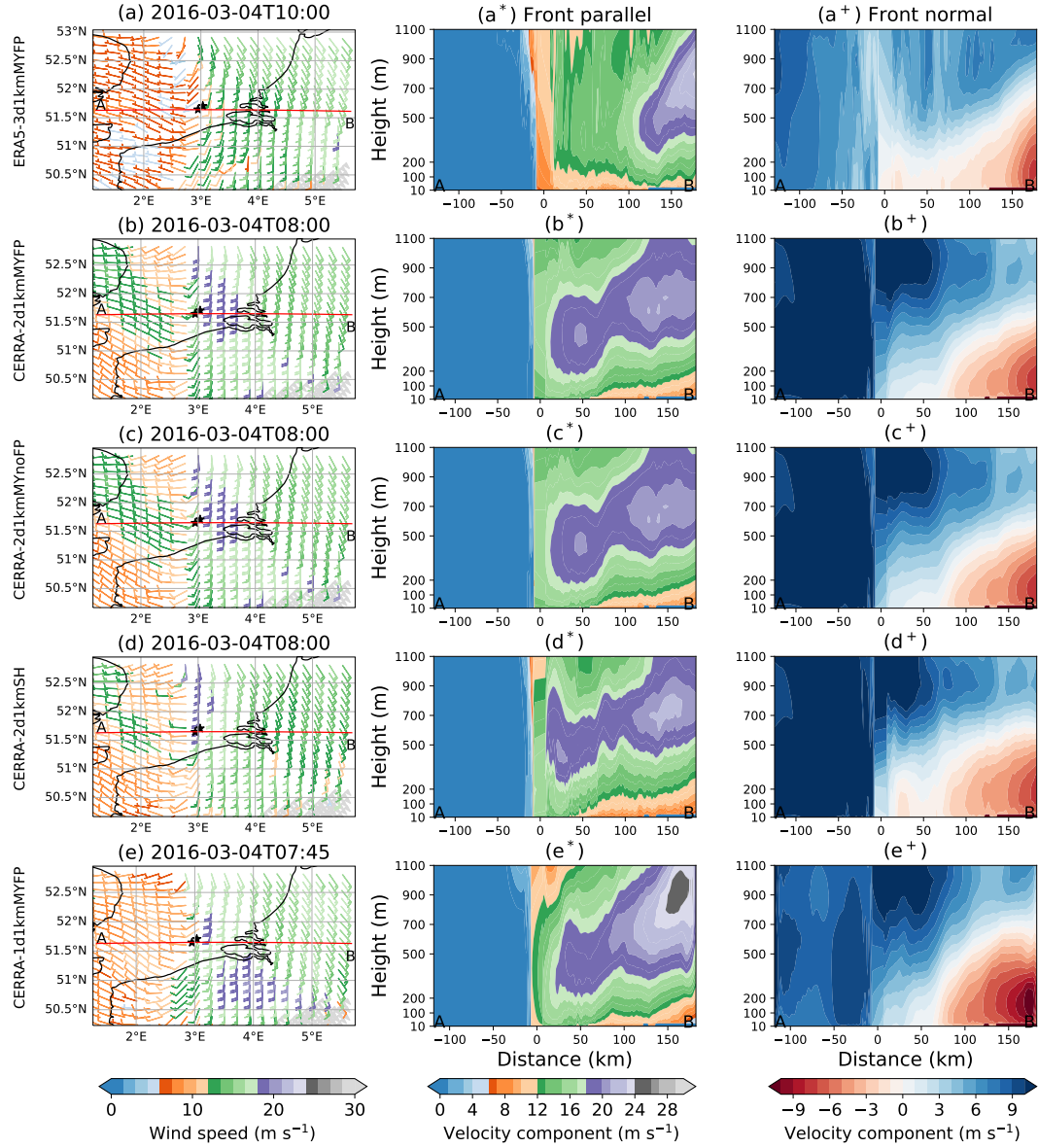
**Figure 9.** Same as Fig. ~~Figure~~ 8, but for case 2, at the ramp instances of the corresponding simulation.
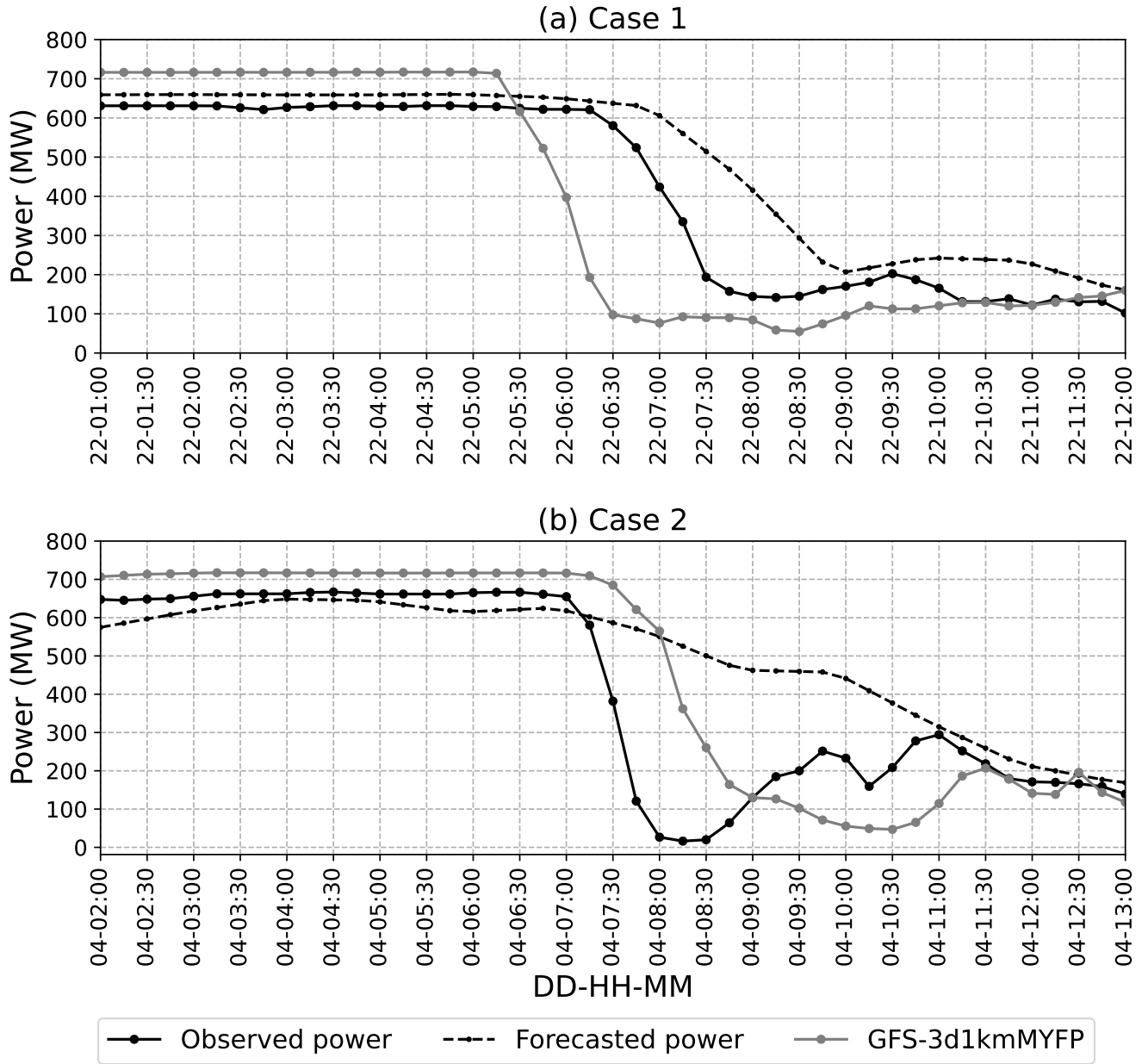
**Figure 10.** A comparison of wind power time series from the GFS-MYFP simulation and the Belgium offshore wind farm production and their Elia day-ahead forecast, during (a) 0100 UTC to 1200 UTC on 21st of February, 2016, for case 1 and (b) during 0200 UTC to 1300 UTC on 4th of March, 2016, for case 2.

from 1200 UTC on the 29th to 1800 UTC on the 30th of January 2017. A comparison between the wind farm-measured and model-simulated wind power time-series is illustrated in Fig. Figure 11 for the three cases.

The results demonstrate that the WRF model successfully simulates the extreme wind power ramps associated with FLLJs, though the specific modeling configurations significantly influence the wind power time series. All simulations capture the strong pre-ramp wind power at the 720 MW rated capacity, likely due to peak wind speeds during the FLLJ, as well as the post-ramp wind power output, which aligns with observed values. The observed strong drop in wind power, representing the extreme ramp, is consistently simulated across cases; however, discrepancies in ramp intensity and timing persist, varying across configurations. The ramp statistics from the four CERRA-based configurations for three cases are computed at a 1-hour time scale and are presented in Table 4. The CERRA-1d1kmMYFP simulation shows superior performance, with the power ramps surpassing 50% within just 1 hour, signifying the extremity of the power ramps. In terms of ramp timing, the simulated ramps are in advance by 2 hours, 45 minutes, and 15 minutes in cases 3, 4, and 5, respectively. This indicates the robustness of CERRA-1d1kmMYFP in accurately capturing ramp timing and intensity for cases 4 and 5. In case 3, while the timing is simulated with a 2-hour lead, the ramp intensity is closely represented compared to other configurations. Other simulations exhibit larger temporal shifts in cases 4 and 5, and underpredicted intensities in cases 3 and 4. Nonetheless, these findings corroborate the robustness of the WRF model in simulating the extreme ramp events associated with the FLLJ, and the better predictability of the CERRA-1d1kmMYFP modeling configuration.

**Table 4.** Overview of the ramp in wind power in terms of intensity (%) and timing (in parenthesis), at a 1-hour time-scale, obtained from the wind power produced by the Belgium offshore wind farm and various CERRA configurations, for cases 3, 4, and 5.

| Model | Case 3 | Case 4 | Case 5 |
|---|---|---|---|
| **Grid-measured** | 67.0 (09:15) | 52.9 (22:00) | 52.7 (06:30) |
| **CERRA-2d1kmMYFP** | 35.2 (06:00) | 53.3 (20:45) | 55.8 (05:15) |
| **CERRA-2d1kmMYnoFP** | 47.1 (08:30) | 33.4 (20:45) | 57.6 (05:30) |
| **CERRA-2d1kmSH** | 52.9 (08:30) | 29.3 (20:30) | 51.7 (06:00) |
| **CERRA-1d1kmMYFP** | 54.2 (07:15) | 50 (21:15) | 58.4 (06:15) |

## 5  Conclusion and recommendations

In this study, we utilized the WRF model to simulate FLLJ and the associated extreme ramp events to analyze the variability in ramp timing, intensity, and jet core strength from a wind energy perspective. We identified five cases where wind power dropped by more than 50% within 1 hour at the Belgium offshore wind farm. Two of these cases were selected for in-depth analysis, while the remaining three were used for generalization. We examined the sensitivity of various model configurations, including different initial and boundary condition datasets, the activation of Fitch wind farm parameterization, and PBL schemes, to understand their impact on the FLLJ and the associated extreme ramp characteristics.
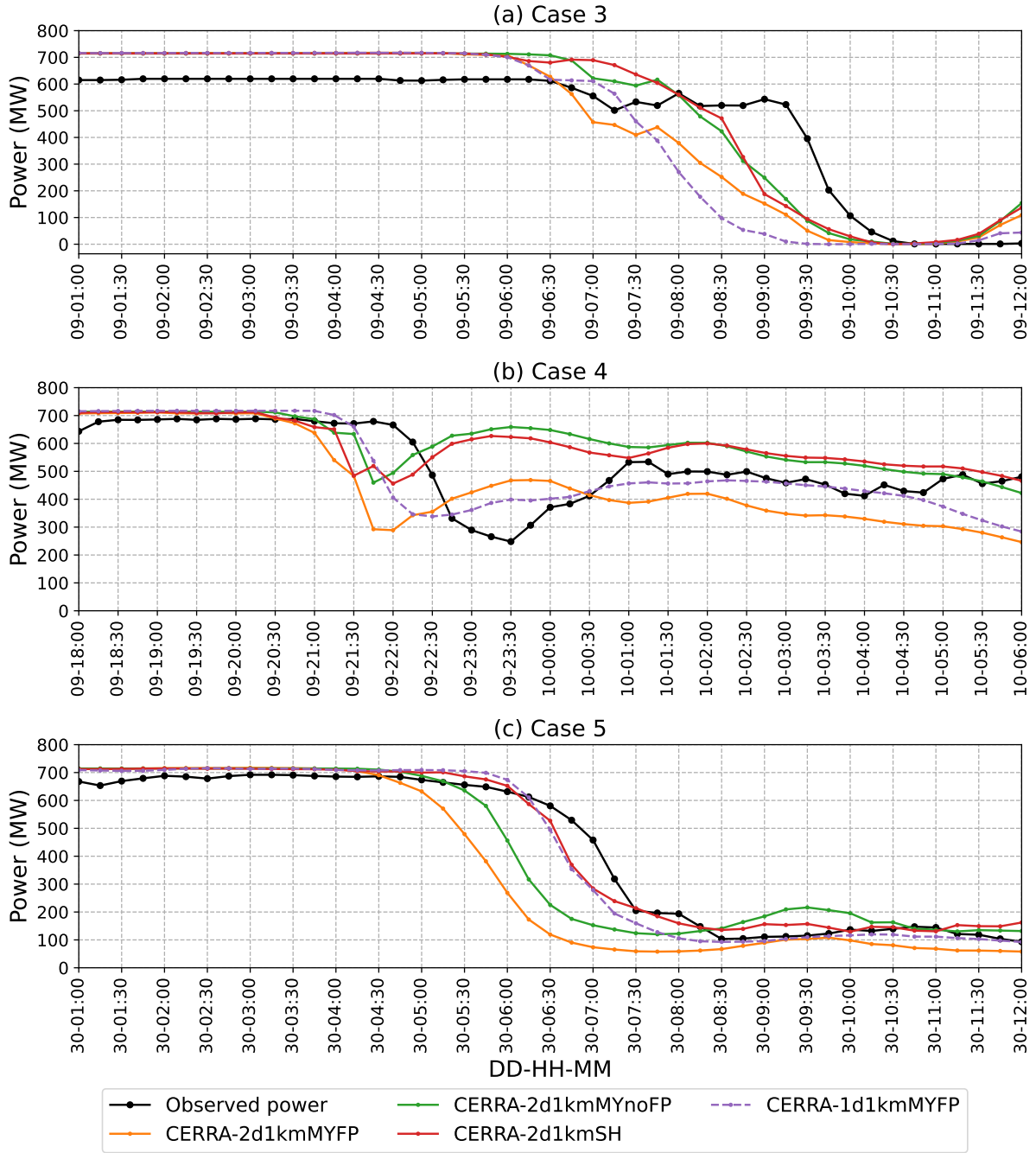
**Figure 11.** A comparison of wind power time series from the CERRA-2d1kmMYFP, CERRA-2d1kmMYnoFP, CERRA-2d1kmSH, and CERRA-1d1kmMYFP configurations and the Belgium offshore wind farm production. (a): during 0100 UTC to 1200 UTC on 9th of February, 2016, for case 3. (b): during 1800 UTC on 9th to 0600 UTC on 10th of January, 2017, for case 4. (d): during 0100 UTC to 1200 UTC on 30th of January, 2017, for case 5.

For basic climatological characterizations of FLLJs and associated extreme ramp events, the ERA5 or CERRA reanalysis datasets are highly beneficial due to their extensive coverage, long-term availability, and high accuracy. However, these datasets do not account for the wake effects of wind farms. To incorporate such effects, using the WRF model or other mesoscale models with an appropriate wind farm parameterization is recommended. Additionally, mesoscale simulations offer advanced diagnostics (e.g., turbulent kinetic energy) and, due to their high spatial resolutions, can effectively resolve coastal effects.

In this study, we found that the chosen modeling parameters significantly influence ramp characteristics and FLLJ synoptic features. The CERRA IC/BCs provided a better representation of the atmospheric flow compared to the ERA5 reanalysis, resulting in more accurate ramp timing, intensity, and FLLJ synoptic features. Activating wind farm parameterization (WFP) significantly impacted wind power output, as WFP models the interaction of individual wind turbines with the atmospheric flow and generates wind wakes in the vicinity of the wind farm. Due to wake generation, wind speeds with WFP were marginally lower than without WFP.

The scale-aware SH scheme produced a stronger FLLJ core at a higher altitude with a more defined and pronounced jet nose compared to the MYNN 2.5 scheme. However, wind speeds below 200 m were lower with the SH scheme than with MYNN 2.5. Finally, the single-domain configuration was more effective in simulating wind power ramp timing and intensity, consistently showing a higher core height than the nested configuration. Additionally, this configuration resulted in higher wind speeds below 200 m, leading to a more diffused jet nose profile.

Analysis of FLLJ synoptic characteristics during ramp instances revealed that the FLLJ phenomenon is primarily driven by the transect normal wind component, aligned parallel to the frontal surface. The heightened wind ramp intensity results from the interplay between minimal transect normal wind speed behind the front and the intensified FLLJ ahead of the front.

We observed that wind power ramp statistics can be reliably simulated using a single domain configuration, as confirmed by three additional cases. If this approach is applicable to other FLLJ and associated extreme ramp events, it could enable accurate simulations with significantly reduced computational costs. In real-time forecasting scenarios, extreme ramp events could be predicted one day in advance with accuracy comparable to reanalysis simulations, enhancing operational efficiency.

Before concluding, it is important to note that the enhanced understanding and forecasting capabilities of Frontal Low-Level Jets (FLLJs) and associated wind power ramp events extend beyond the wind energy sector. Improved insights into FLLJs are also crucial for grid operators and energy market regulators, who need to ensure system stability and manage the economic implications of sudden fluctuations in power generation.

**Appendix A:  Additionl case studies**

This section presents a wind power time-series measured by the Belgium offshore wind farms during the three additional cases and the corresponding synoptic charts.
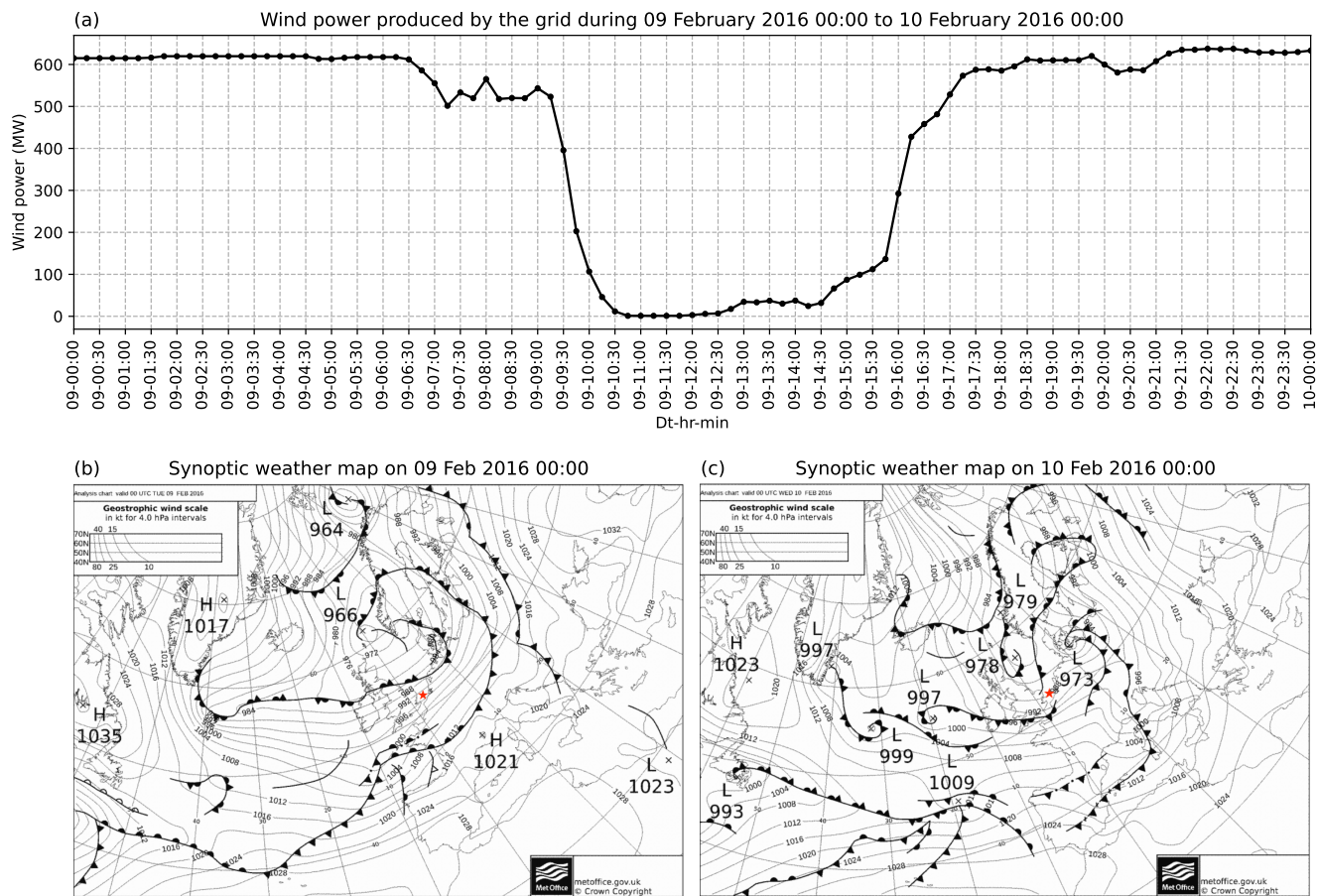
**Figure A1.** Same as Fig. Figure 1, but for case 3. (a) The time series of wind power produced by the Belgian offshore wind farms, from 0000 UTC on the 9th to 1000 UTC on the 10th of February 2016, which depicts the extreme power ramp. (b) Synoptic weather maps on 0000 UTC of 9th February 2016 and (c) 0000 UTC of 10th February 2016, illustrating a cold front passing over the Belgium offshore wind farm (illustrated with red star).

## A1    Case 3

On 9th February 2016, the wind farm experienced a 67% drop in its measured wind power within 1 hour, beginning from 0915 UTC, as shown in section A1(top panel). The farm is seen producing a maximum wind power of 600 MW, for more than 9 hours period before experiencing the ramp event, suggesting the occurrence of peak wind speed during this period. Coinciding, the synoptic weather maps at 0000 UTC on the 9th and 10th of February (bottom left and right panels of section A1, respectively) clearly illustrate a cold front (dark line with triangles pointing the direction of frontal movement) overpassing the wind farm.

525
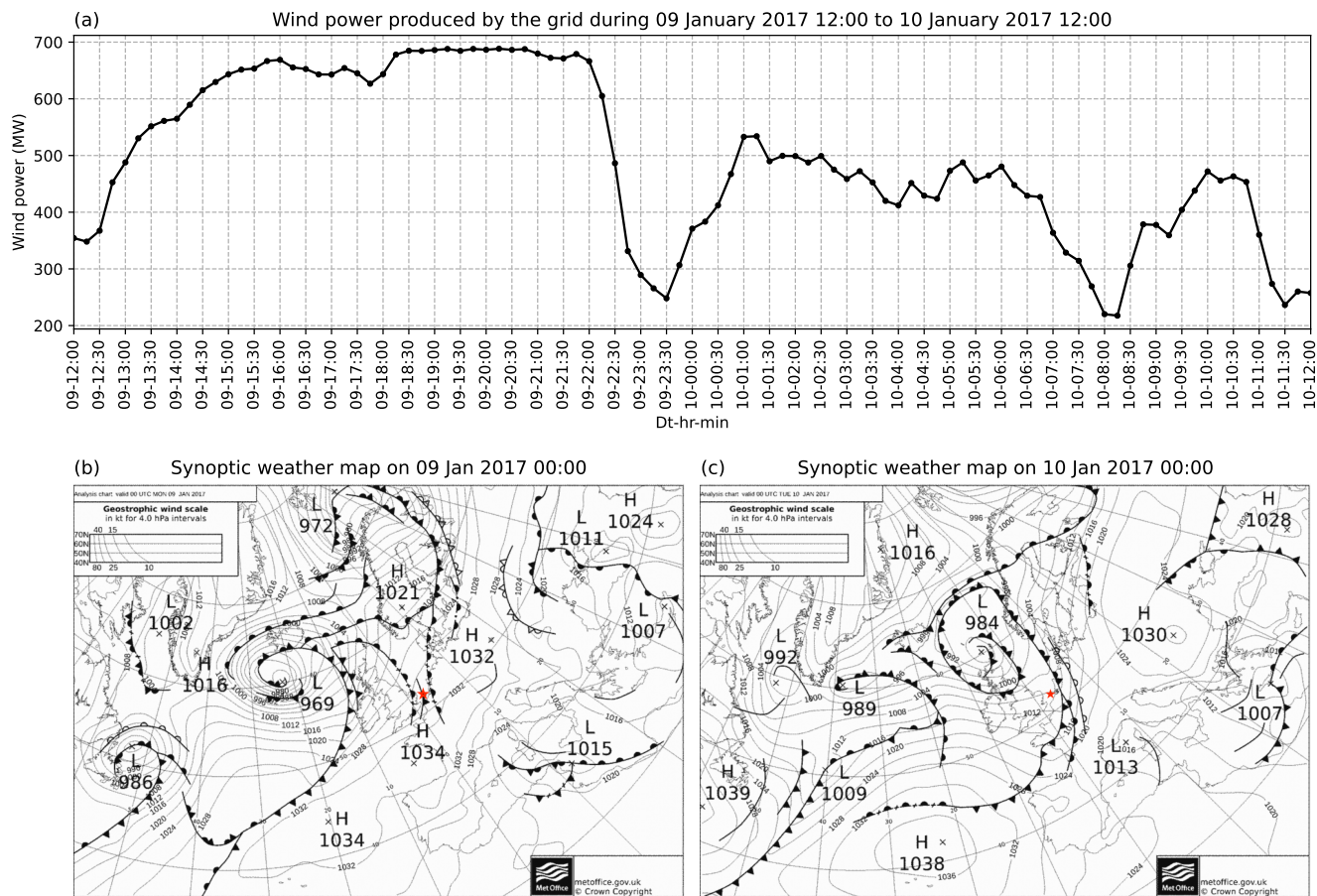
**Figure A2.** Same as Fig. Figure 1, but for case 4. (a) The time series of wind power produced by the Belgian offshore wind farms, from 1200 UTC on the 9th to 1200 UTC on the 10th of January 2017, which depicts the extreme power ramp. (b) Synoptic weather maps on 0000 UTC of 9th January 2017 and (c) 0000 UTC of 10th January 2017, illustrating a cold front passing over the Belgium offshore wind farm (illustrated with red star).

## A2 Case 4

On 9th January 2017, the wind farm experienced a 52% drop in it's measured wind power within 1 hour, beginning from 2200 UTC, as shown in section A2(top panel). The farm is seen producing a maximum wind power of 690 MW, for more than 4 hours period before experiencing the ramp event, suggesting the occurrence of peak wind speed during this period. Coinciding, the synoptic weather maps at 0000 UTC on 9th and 10th of January (bottom left and right panels of section A2, respectively) clearly illustrating a cold front (dark line with triangles pointing the direction of frontal movement) overpassing the wind farm.
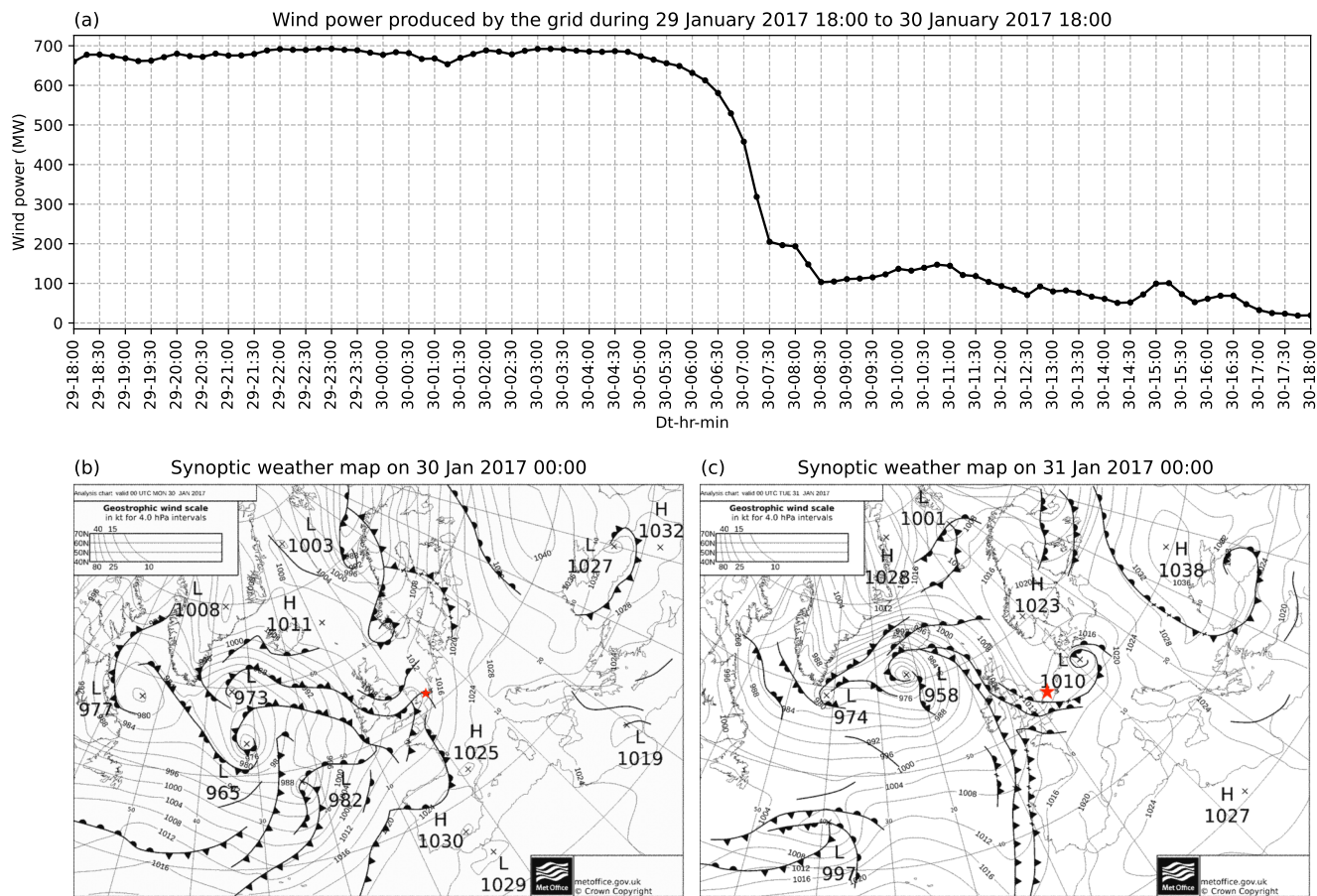
**Figure A3.** Same as Fig. Figure 1, but for case 5. (a) The time series of wind power produced by the Belgian offshore wind farms, from 1800 UTC on the 29th to 1800 UTC on the 30th of January 2017, depicts the extreme power ramp. (b) Synoptic weather maps on 0000 UTC of 30th January 2017 and (c) 0000 UTC of 31st January 2017, illustrating a cold front passing over the Belgium offshore wind farm (illustrated with red star).

## A3    Case 5

535    On 30th January 2017, the wind farm experienced a 52% drop in its measured wind power within 1 hour, beginning from 0630 UTC, as shown in section A3(top panel). The farm is seen producing a maximum wind power of 670 MW, for more than 12 hours period before experiencing the ramp event, suggesting the occurrence of peak wind speed during this period. Coinciding, the synoptic weather maps at 0000 UTC on the 30th and 31st of January (bottom left and right panels of section A3, respectively) clearly illustrate a cold front (dark line with triangles pointing the direction of frontal movement) overpassing the

540    wind farm.

## Appendix B:  Sensitivity to the vertical levels

We have examined the influence of vertical levels on the simulations by selecting 100 vertical levels, with approximately 27 vertical levels within the first 1 km of height. Using this vertical resolution and the CERRA-1km1dMYFP configuration, the first two cases were simulated. In our study, the choice of 50 vertical levels was adopted from Nunalee and Basu (2014), where in the case of coastal LLJs, the authors reported reduced jet strength and lower jet core height with increased vertical levels, deviating from the observations. Similar to their findings, we noticed that vertical levels exert considerable influence on the ramp timing and marginal influence on the ramp intensity, as shown in Fig. B1. However, we also recognize the limitations of our findings, since they are based on two simulations focused specifically on FLLJ cases.

## Appendix C:  Sensitivity to the spin-up time

To evaluate the sensitivity of model accuracy to the choice of spin-up time, we conducted simulations for two cases using the CERRA-1d1kmMYFP configuration: one with a 6-hour spin-up (original simulation duration) and another with a 12-hour spin-up (starting 6 hours prior to the original duration). Figure C1 presents wind power time-series from both simulations, compared with the measured power output for Cases 1 and 2. The results show that the wind power output from both simulations is identical, indicating that a 6-hour spin-up is sufficient for the development of the FLLJ cases. However, it is highly unlikely for simulations initialized with different IC/BCs to produce identical results. To further verify this, we computed the wind speed difference between the two simulations and plotted their time-height cross-section at the LOT2 location, for cases 1 and 2, as shown in Fig. C2. From the illustration, it was found that the wind speed differences are infinitesimal, in the range of $\pm 0.1$ m s$^{-1}$ throughout, and occasionally $\pm 1$ m s$^{-1}$, thus the wind power outputs from the two simulations also remain identical. These findings confirm that the chosen 6-hour spin-up duration is adequate for accurately capturing the dynamics of these events.

## Appendix D:  Comparison between driving data

This section presents a comparison between the driving data, namely ERA5, CERRA, and GFS, for cases 1 and 2.

### D1    Wind speed time-series

The ERA5 reanalysis provides 100 m level wind speed at hourly intervals. In contrast, the CERRA reanalysis provides 100 m wind speed at three hourly analyses and hourly forecasts. To mimic a continuous hourly dataset, we procured analysis every three hours and the forecast for the next two hours. On the other hand, 100 m wind speed does not available in GFS forecasts, thus we chose 975 hPa wind speed available every 3 hours. A comparison between these two wind speed datasets along with the lidar observations at the LOT2 location are presented in Figure D1.

CERRA and ERA5 provide wind speeds at 100 m above ground level, while GFS provides wind speeds at the 975 hPa pressure level. However, four of the five wind turbine types operating in the wind farm have hub heights below 100 m, making
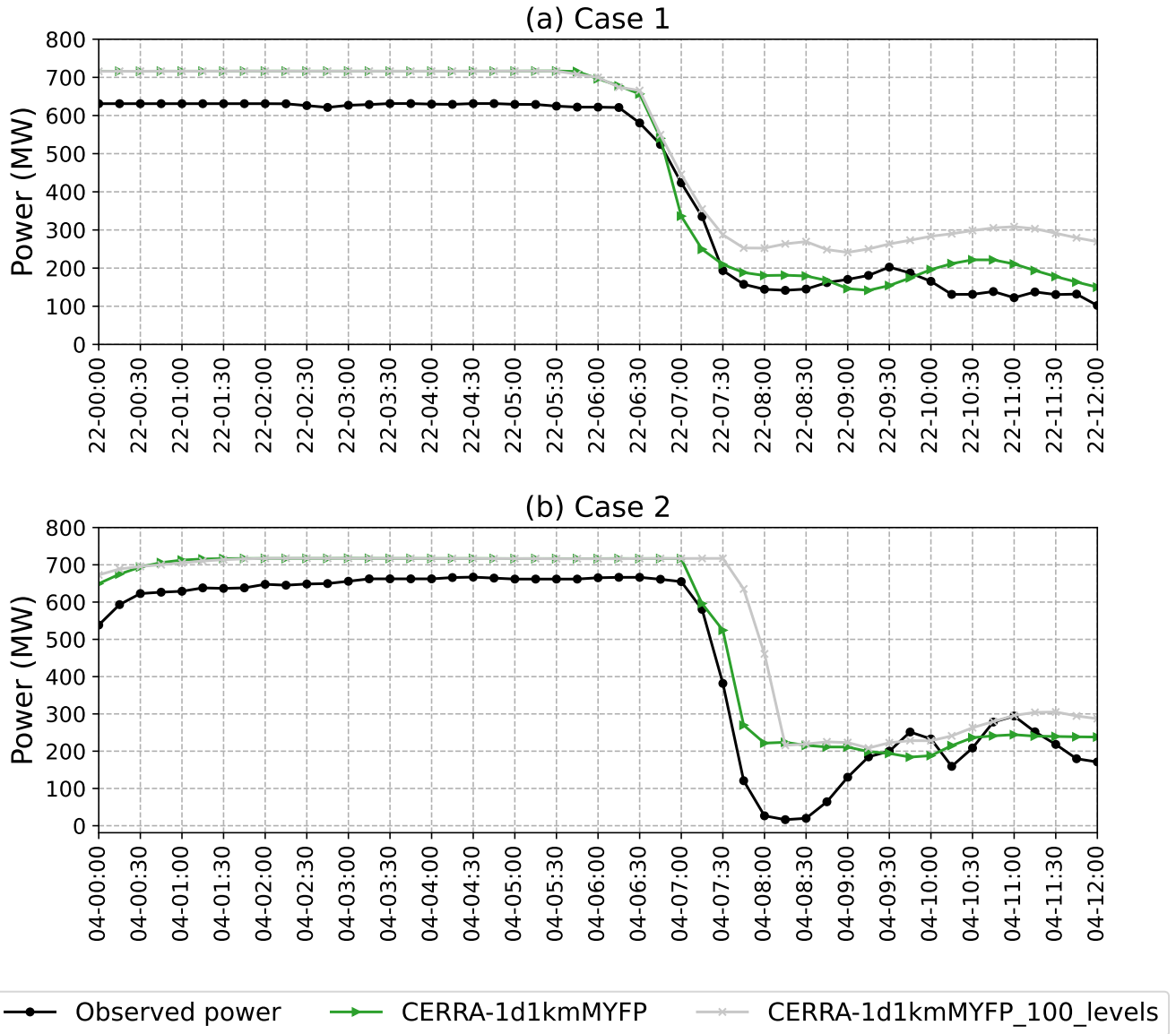
**Figure B1.** A comparison of wind power time series from the WRF model simulations of CERRA-1d1kmMYFP configuration, with 50 vertical levels and 100 vertical levels, and the Belgium offshore wind farm production. (a) During 0100 UTC to 1200 UTC on the 21st of February, 2016, for case 1. (b) During 0200 UTC to 1300 UTC on the 4th of March, 2016, for case 2.
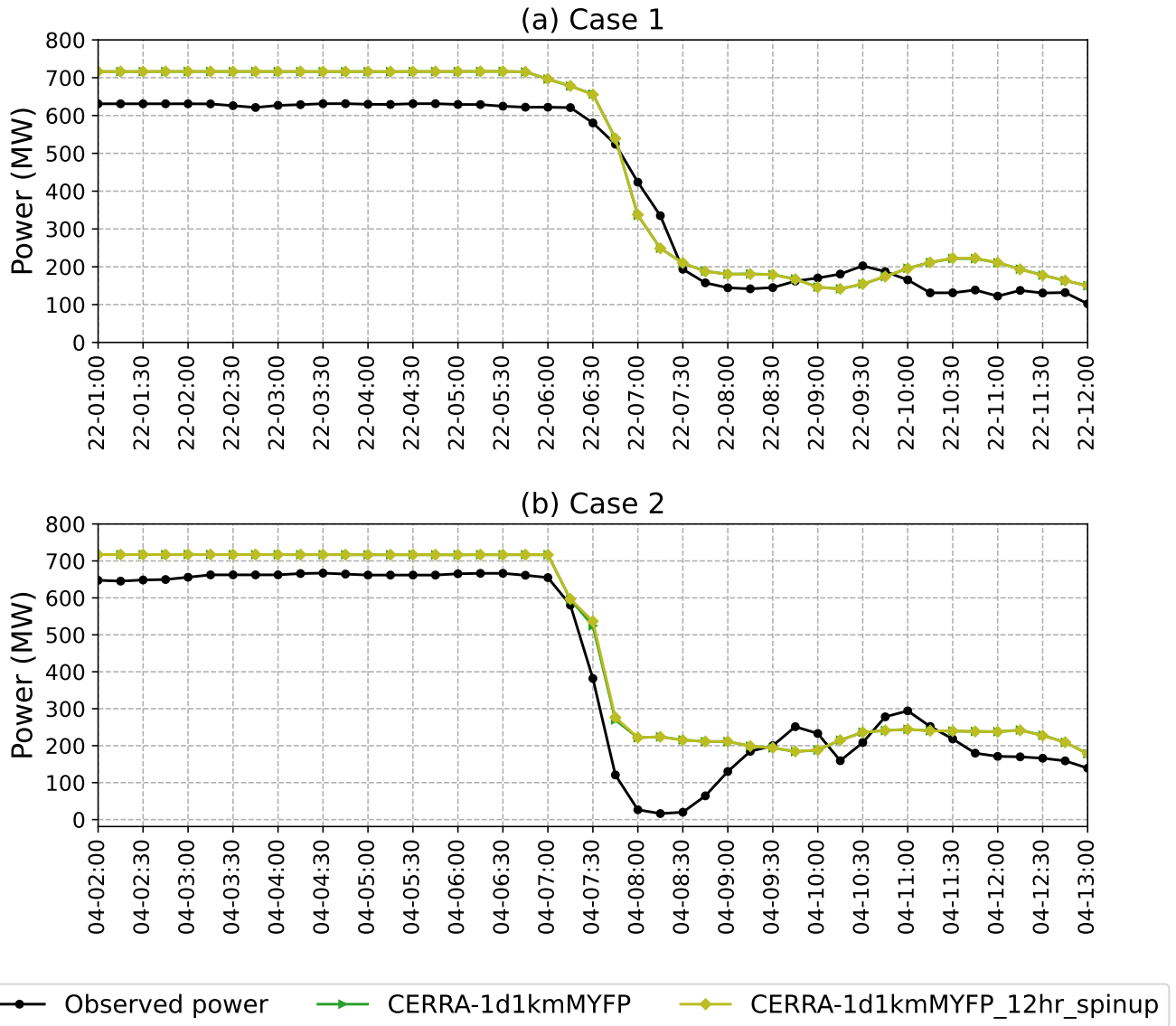
**Figure C1.** A comparison of wind power time series from the WRF model simulations of CERRA-1d1kmMYFP configuration, one with 6 hr spin-up and another with 12 hr spin-up, and the Belgium offshore wind farm production. (a) Dring 0100 UTC to 1200 UTC on 21st of February, 2016, for case 1. (b) During 0200 UTC to 1300 UTC on 4th of March, 2016, for case 2.
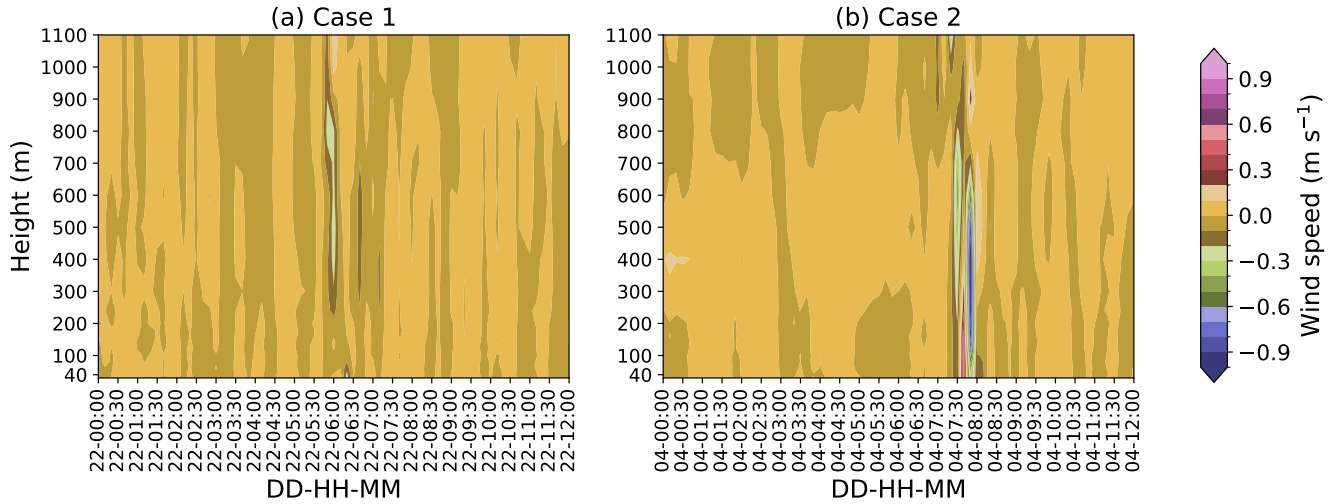
**Figure C2.** Time-height cross-section of wind speed difference between the CERRA-1d1kmMYFP simulations with 6hr and 12hr spin-up, at the LOT2 location for cases 1 and 2.

it challenging to accurately approximate wind power production using the forcing datasets. The ERA5 reanalysis exists at a temporal resolution of 1 hour and a spatial resolution of 0.25°, the CERRA analysis exists at a temporal resolution of 3 hours (while the forecast data has a temporal resolution of 1 hour) and a spatial resolution of 5.5 km, and the GFS forecast exists at a temporal resolution of 3 hours (archives 2016-17 exist at 3-hourly intervals, while the current data available at 1-hourly intervals) and a spatial resolution of 0.25°. Due to these coarse spatial resolutions, the entire wind farm fits within a single grid cell for ERA5 and GFS, while only a few grid cells from CERRA cover the wind farm. These spatial limitations hinder the representation of the wind power output generated by 182 turbines within the wind farm. This is critical, as the heterogeneity in turbine locations and wind conditions cannot be resolved with the coarser spatial scales of the forcing data. The GFS follows the overall trend of observed wind speeds, it exhibits a clear overestimation in magnitude. Moreover, the coarse temporal resolution of GFS makes it challenging to quantify ramp statistics, particularly as extreme ramps associated with frontal low-level jets (FLLJs) occur on scales of 15 minutes to 1 hour. This further demonstrates that dynamical downscaling is indispensable for understanding extreme wind ramps at sub-hourly scales, which are critical for wind power applications.

## D2 Wind speed profiles

The ERA5 and CERRA reanalysis datasets provide model-level wind speed data, which could serve as wind speed profiles. However, we intend to visualize the wind speed profiles from the dataset we used as IC/BCs, which are indeed pressure-level datasets. In doing so, we extracted the profiles from the metfiles of ERA5 and CERRA runs' parent domain. The profiles are illustrated in Figure D2, for cases 1 and 2.
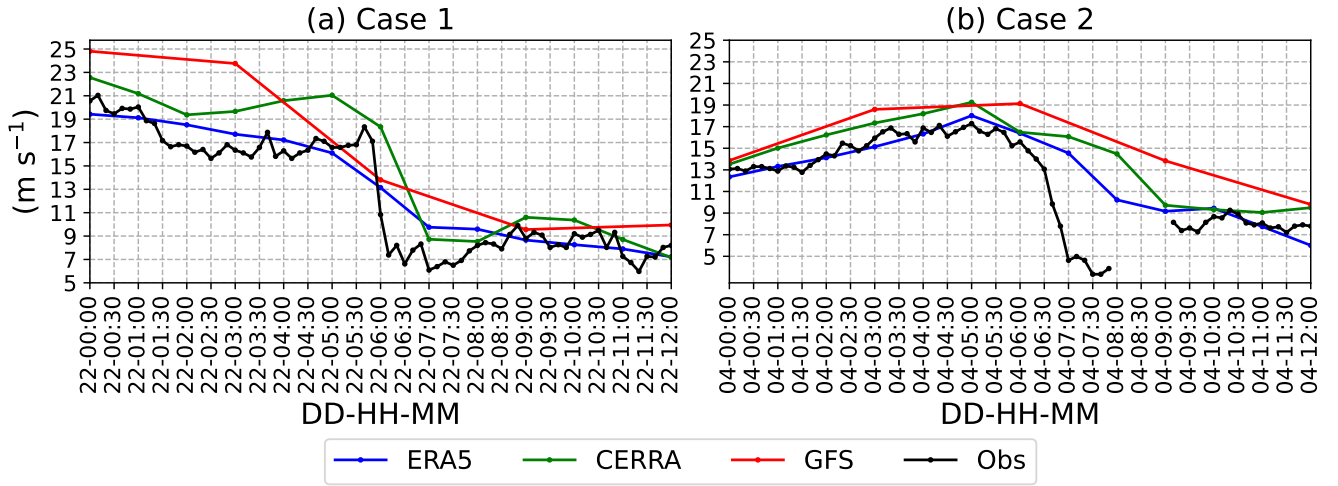
**Figure D1.** A comparison of 100 m wind speed time series from lidar observations, ERA5, and CERRA reanalysis. The GFS wind speed time series is extracted at 975 hPa level. (a) During 0100 UTC to 1200 UTC on the 21st of February, 2016, for case 1. (b) During 0200 UTC to 1300 UTC on the 4th of March, 2016, for case 2.
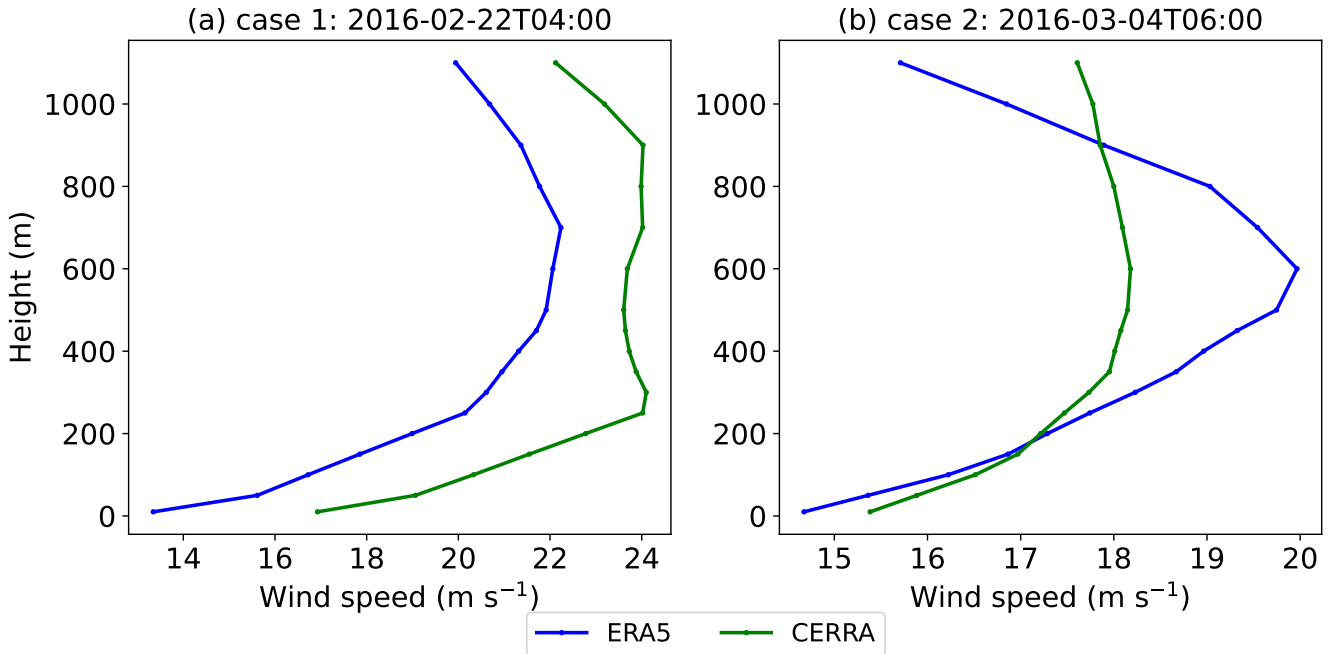
**Figure D2.** A comparison of wind speed profiles from the ERA5 and CERRA reanalysis, for case 1 (a) during 0400 UTC on 22nd Feb 2016 and case 2 (b) during 0600 UTC on 4th Mar 2016, at LOT2 location.

## Appendix E:  Time-height cross-section of wind speed from the WRF runs

This section presents the time-height cross-section of wind speed from the five WRF runs along with the lidar observations at
590   the LOT2 location, for cases 1 and 2.

## Appendix F:  Wind farm wakes

This section presents a comparison of horizontal wind speed contours at 100 m level from the CERRA-2d1kmMYFP and
CERRA-2d1kmMYnoFP simulations, at different time instances, for cases 1 and 2.

*Data availability.*  The ERA5 and CERRA reanalysis are downloaded from ECMWF CDO, available at https://cds.climate.copernicus.eu/
595   cdsapp#!/search?type=dataset.

*Author contributions.*  HB is responsible for data analysis, model simulations, and manuscript writing. SB and GL contributed to manuscript
organization, text revision, and result discussions.

*Competing interests.*  Some authors are members of the editorial board of journal Wind Energy Science.

*Acknowledgements.*  The authors acknowledge the use of computational resources of the DelftBlue supercomputer, provided by Delft High
600   Performance Computing Centre (https://www.tudelft.nl/dhpc). This EU-SCORES project has received funding from the European Union's
Horizon 2020 research and innovation programme under grant agreement No 101036457. We extend our gratitude to Elia for publicly sharing
the Belgian offshore wind power production data. We also thank TNO for providing the LiDAR observed data.
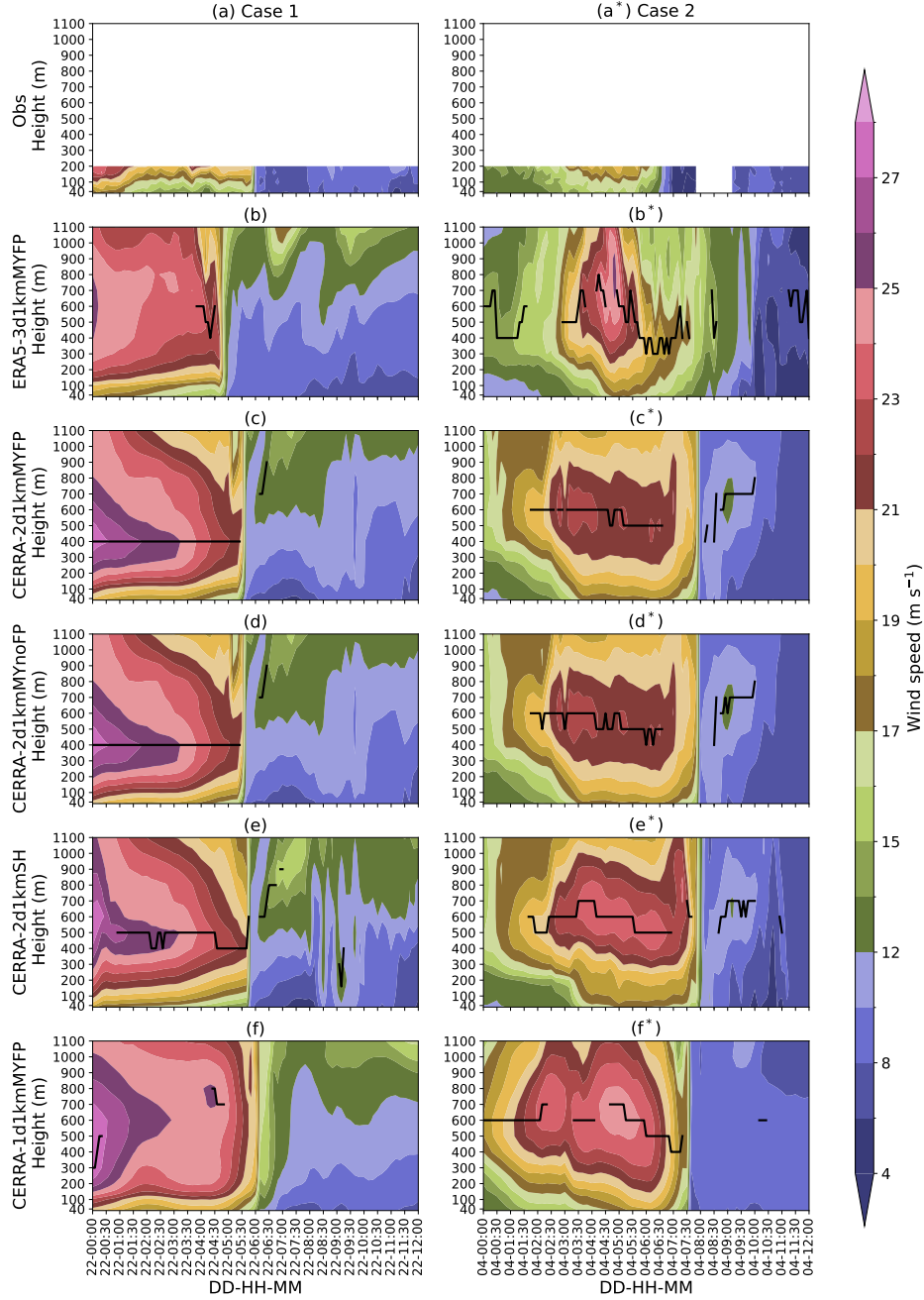
**Figure E1.** Time-height cross-sections of wind speed at the LOT2 location for cases 1 and 2. (a-a*) Wind speed from lidar observations. (b-b* to f-f*) Wind speed from the WRF simulations, ERA5-3d1kmMYFP, CERRA-2d1kmMYFP, CERRA-2d1kmMYnoFP, CERRA-2d1kmSH, and CERRA-1d1kmMYFP. A solid black line spanning through the time series indicates the presence of low-level jet.
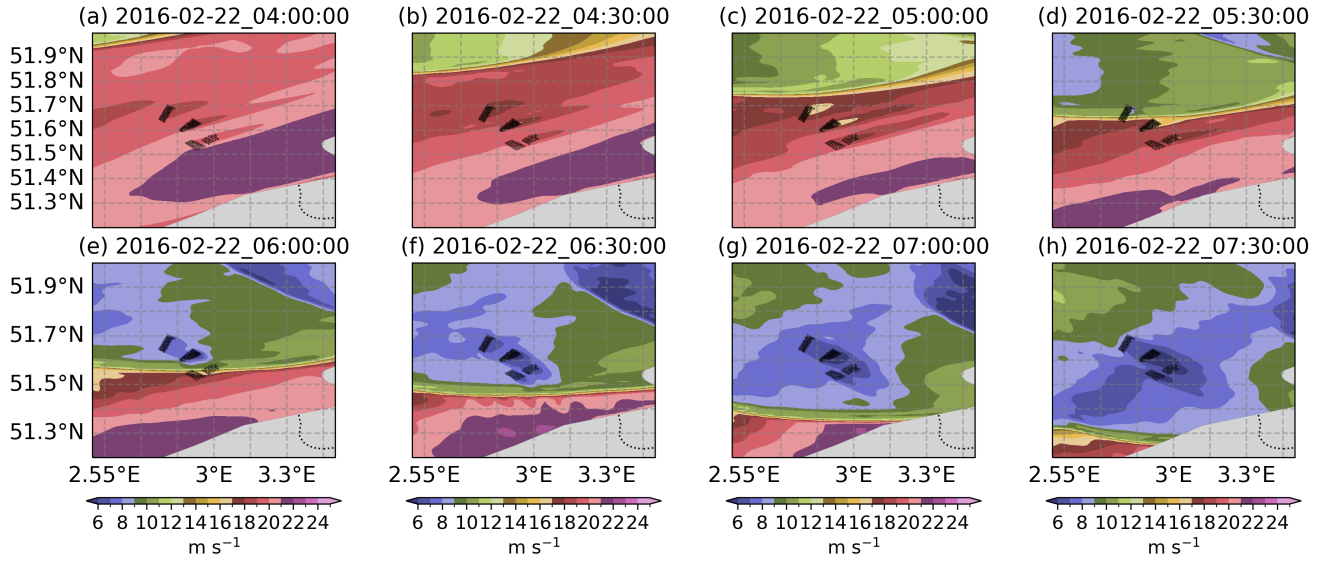
**Figure F1.** Illustrations of 100 m level wind speed from the CERRA-2d1kmMYFP simulation for case 1, at the instance of every 30 minutes during 0400 UTC to 0730 UTC on 22nd February 2016.
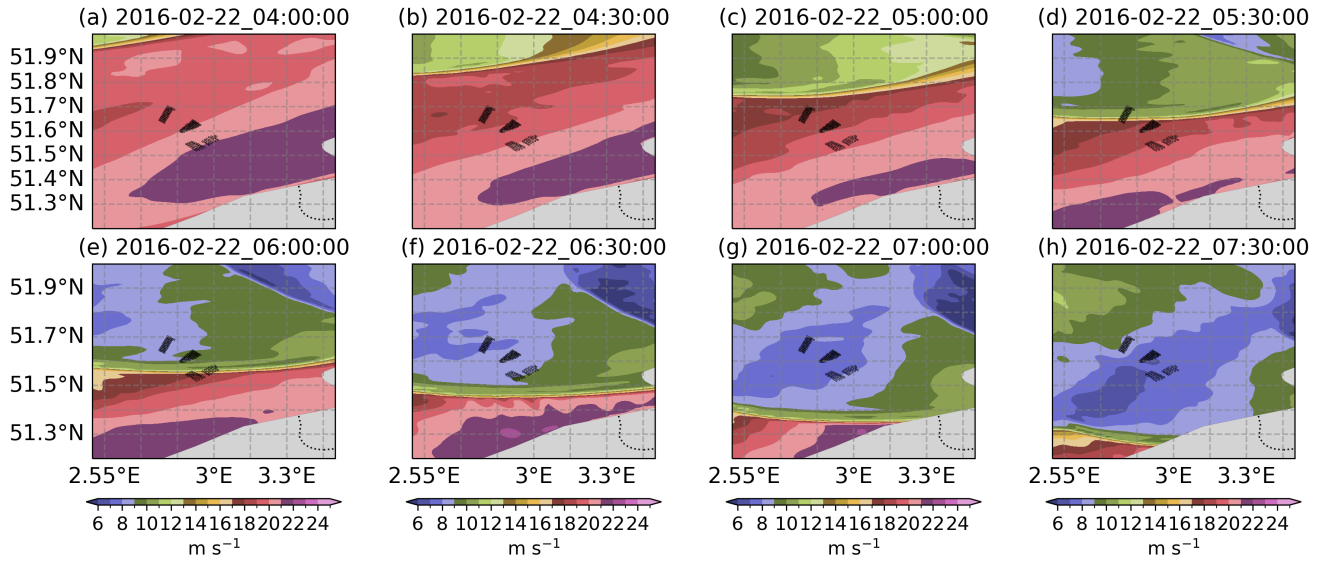
**Figure F2.** Same as Figure F1, but from the 2d1kmMYnoFP simulation.
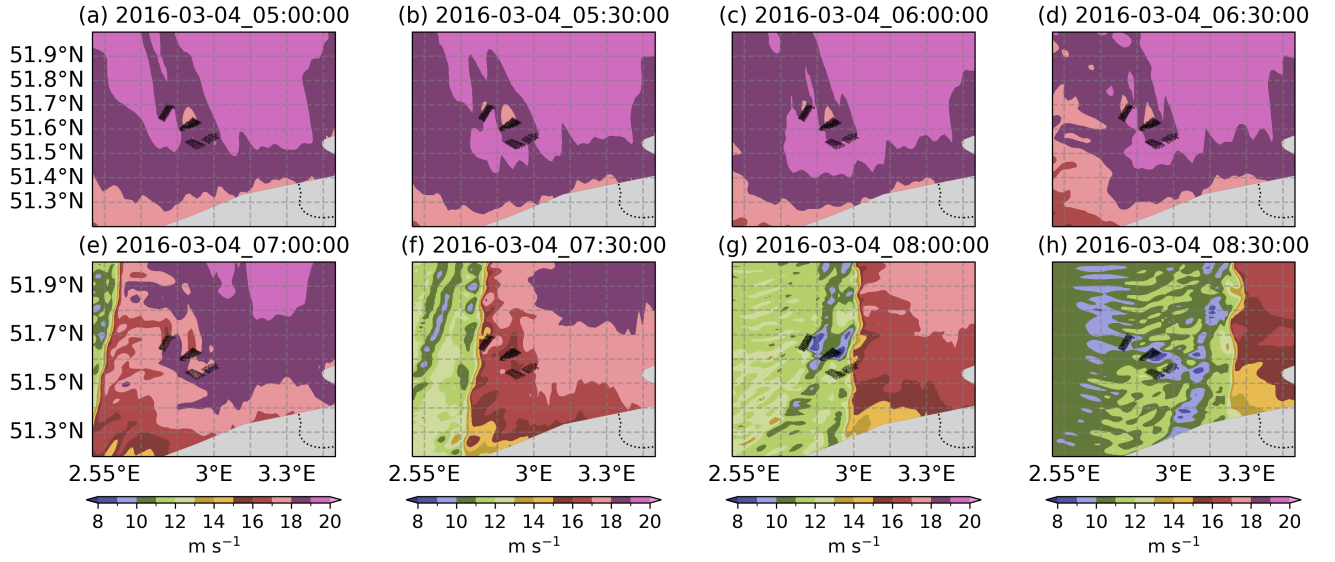
**Figure F3.** Illustrations of 100 m level wind speed from the CERRA-2d1kmMYFP simulation for case 2, at the instance of every 30 minutes from 0500 UTC to 0830 UTC on 4th March 2016.
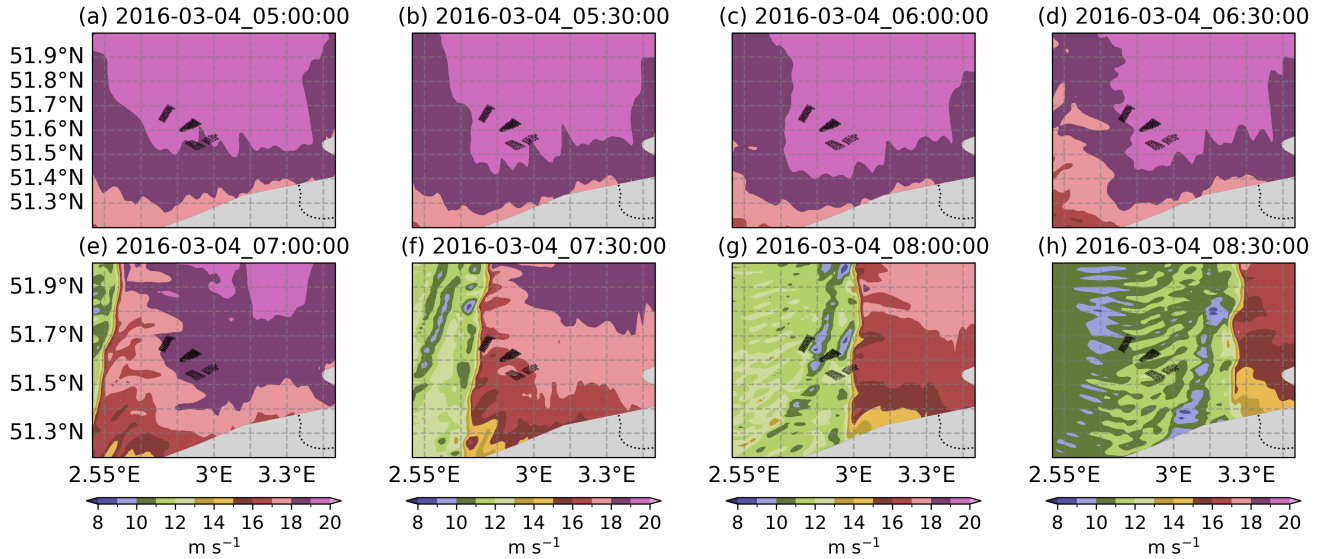
**Figure F4.** Same as Figure F3, but from the 2d1kmMYnoFP simulation.

# References

Aird, J. A., Barthelmie, R. J., Shepherd, T. J., and Pryor, S. C.: WRF-simulated low-level jets over Iowa: characterization and sensitivity studies, Wind Energy Sci., 6, 1015–1030, 2021.

Arthur, R. S., Mirocha, J. D., Marjanovic, N., Hirth, B. D., Schroeder, J. L., Wharton, S., and Chow, F. K.: Multi-Scale Simulation of Wind Farm Performance during a Frontal Passage, Atmosphere, 11, 245, 2020.

Blackadar, A. K.: Boundary layer wind maxima and their significance for the growth of nocturnal inversions, Bulletin of the American Meteorological Society, 38, 283–290, 1957.

Bonner, W. D.: CLIMATOLOGY OF THE LOW LEVEL JET, Mon. Weather Rev., 96, 833–850, 1968.

Brill, K. F., Uccellini, L. W., Burkhart, R. P., Warner, T. T., and Anthes, R. A.: Numerical simulations of a transverse indirect circulation and low-level jet in the exit region of an upper-level jet, Journal of the atmospheric sciences, 42, 1306–1320, 1985.

Browning, K. A.: Mesoscale Structure of Rain Systems in the British Isles, Journal of the Meteorological Society of Japan. Ser. II, 52, 314–327, 1974.

Browning, K. A.: Conceptual Models of Precipitation Systems, Weather Forecast., 1, 23–41, 1986.

Browning, K. A. and Harrold, T. W.: Air motion and precipitation growth at a cold front, Quart. J. Roy. Meteor. Soc., 96, 369–389, 1970.

Browning, K. A. and Monk, G. A.: A Simple Model for the Synoptic Analysis of Cold Fronts, Quart. J. Roy. Meteor. Soc., 108, 435–452, 1982.

Browning, K. A. and Pardoe, C. W.: Structure of low-level jet streams ahead of mid-latitude cold fronts, Quart. J. Roy. Meteor. Soc., 099, 619–638, 1973.

Browning, K. A., Jerrett, D., Nash, J., Oakley, T., and Roberts, N. M.: Cold frontal structure derived from radar wind profilers, Meteorol. Appl., 5, 67–74, 1998.

Carvalho, D., Rocha, A., Gómez-Gesteira, M., and Santos, C. S.: WRF wind simulation and wind energy production estimates forced by different reanalyses: Comparison with observed data for Portugal, Applied Energy, 117, 116–126, 2014.

Chen, Y.-L., Chen, X. A., and Zhang, Y.-X.: A diagnostic study of the low-level jet during TAMEX IOP 5, Monthly weather review, 122, 2257–2284, 1994.

Cheneka, B. R., Watson, S. J., and Basu, S.: Associating Synoptic-Scale Weather Patterns with Aggregated Offshore Wind Power Production and Ramps, Energies, 14, 3903, 2021.

Cheng, W. Y. Y., Liu, Y., Liu, Y., Zhang, Y., Mahoney, W. P., and Warner, T. T.: The impact of model physics on numerical wind forecasts, Renewable Energy, 55, 347–356, 2013.

Cutler, N., Kay, M., Jacka, K., and Nielsen, T. S.: Detecting, categorizing and forecasting large ramps in wind farm power output using meteorological observations and WPPT, Wind Energy, 10, 453–470, 2007.

Dalton, A., Bekker, B., and Kruger, A.: Wind power variability during the passage of cold fronts across South Africa, J. Energy South. Afr., 30, 52–67, 2019.

de Linaje, N. G.-A., Mattar, C., and Borvarán, D.: Quantifying the wind energy potential differences using different WRF initial conditions on Mediterranean coast of Chile, Energy, 188, 116 027, 2019.

Demirdjian, R., Norris, J. R., Martin, A., and Martin Ralph, F.: Dropsonde Observations of the Ageostrophy within the Pre-Cold-Frontal Low-Level Jet Associated with Atmospheric Rivers, Mon. Weather Rev., 148, 1389–1406, 2020.

Dreef, J.: Simulating Frontal Low Level Jets and Quantifying their Impact on Wind Energy Production, 2019.

640   Drew, D. R., Cannon, D. J., Barlow, J. F., Coker, P. J., and Frame, T. H. A.: The importance of forecasting regional wind power ramping: A case study for the UK, Renew. Energy, 114, 1201–1208, 2017.

Drew, D. R., Barlow, J. F., and Coker, P. J.: Identifying and characterising large ramps in power output of offshore wind farms, Renewable Energy, 127, 195–203, 2018.

Dudhia, J.: A Nonhydrostatic Version of the Penn State–NCAR Mesoscale Model: Validation Tests and Simulation of an Atlantic Cyclone
645   and Cold Front, Mon. Weather Rev., 121, 1493–1513, 1993.

Ela, E. and Kirby, B.: ERCOT event on February 26, 2008: Lessons learned, Tech. rep., National Renewable Energy Lab.(NREL), Golden, CO (United States), 2008.

European Union: Directive (EU) 2018/2001 of the European Parliament and of the Council of 11 December 2018 on the promotion of the use of energy from renewable sources, https://eur-lex.europa.eu/eli/dir/2018/2001/oj, accessed on 18 October 2023, 2018.

650   Fitch, A. C., Olson, J. B., Lundquist, J. K., Dudhia, J., Gupta, A. K., Michalakes, J., and Barstad, I.: Local and mesoscale impacts of wind farms as parameterized in a mesoscale NWP model, Mon. Weather Rev., 140, 3017–3038, 2012.

Freedman, J., Markus, M., and Penc, R.: Analysis of West Texas Wind Plant Ramp-up and Ramp-down Events, AWS Truewind, LLC, pp. 251–278, 2008.

Gallego-Castillo, C., Cuerva-Tejero, A., and Lopez-Garcia, O.: A review on the recent history of wind power ramp forecasting, Renewable
655   Sustainable Energy Rev., 52, 1148–1157, 2015.

Gerber, H., Chang, S., and Holt, T.: Evolution of a marine boundary-layer jet, Journal of the Atmospheric Sciences, 46, 1312–1326, 1989.

Gevorgyan, A.: A case study of low-level jets in Yerevan simulated by the WRF model, Journal of Geophysical Research: Atmospheres, 123, 300–314, 2018.

Gualtieri, G.: Analysing the uncertainties of reanalysis data used for wind resource assessment: A critical review, Renewable and Sustainable
660   Energy Reviews, 167, 112 741, 2022.

Hahmann, A. N., Sīle, T., Witha, B., Davis, N. N., Dörenkämper, M., Ezber, Y., García-Bustamante, E., González-Rouco, J. F., Navarro, J., Olsen, B. T., and Söderberg, S.: The making of the New European Wind Atlas – Part 1: Model sensitivity, Geosci. Model Dev., 13, 5053–5078, 2020.

Hallgren, C., Aird, J. A., Ivanell, S., Körnich, H., Barthelmie, R. J., Pryor, S. C., and Sahlée, E.: Brief communication: On the definition of
665   the low-level jet, Wind Energy Science, 8, 1651–1658, 2023.

Haupt, S. E., Mahoney, W. P., and Parks, K.: Wind Power Forecasting, in: Weather Matters for Energy, edited by Troccoli, A., Dubus, L., and Haupt, S. E., pp. 295–318, Springer New York, New York, NY, 2014.

Hawbecker, P., Basu, S., and Manuel, L.: Realistic simulations of the July 1, 2011 severe wind event over the Buffalo Ridge Wind Farm, Wind Energy, 20, 1803–1822, 2017.

670   Hersbach, H., Bell, B., Berrisford, P., Hirahara, S., Horányi, A., Muñoz-Sabater, J., Nicolas, J., Peubey, C., Radu, R., Schepers, D., et al.: The ERA5 global reanalysis, Quarterly Journal of the Royal Meteorological Society, 146, 1999–2049, 2020.

Hong, S.-Y., Dudhia, J., and Chen, S.-H.: A revised approach to ice microphysical processes for the bulk parameterization of clouds and precipitation, Monthly weather review, 132, 103–120, 2004.

Iacono, M. J., Delamere, J. S., Mlawer, E. J., Shephard, M. W., Clough, S. A., and Collins, W. D.: Radiative forcing by long-lived greenhouse
675   gases: Calculations with the AER radiative transfer models, Journal of Geophysical Research: Atmospheres, 113, 2008.

Jahn, D. E., Takle, E. S., and Gallus, W. A.: Improving Wind-Ramp Forecasts in the Stable Boundary Layer, Bound.-Layer Meteorol., 163, 423–446, 2017.

Jiménez, P. A., Dudhia, J., González-Rouco, J. F., Navarro, J., Montávez, J. P., and García-Bustamante, E.: A revised scheme for the WRF surface layer formulation, Monthly weather review, 140, 898–918, 2012.

680    Jiménez, P. A., Navarro, J., Palomares, A. M., and Dudhia, J.: Mesoscale modeling of offshore wind turbine wakes at the wind farm resolving scale: A composite-based analysis with the Weather Research and Forecasting model over Horns Rev, Wind Energy, 18, 559–566, 2015.

Kain, J. S.: The Kain–Fritsch convective parameterization: an update, Journal of applied meteorology, 43, 170–181, 2004.

King, J., Andy, C., and Bri-Mathias, H.: Validation of power output for the WIND Toolkit, Tech. rep., Technical report NREL/TP-5D00-61714", National Renewable Energy Lab.(NREL), Golden, CO (United States), 2014.

685    Kotroni, V. and Lagouvardos, K.: Low-level jet streams associated with atmospheric cold fronts: Seven case studies from the Fronts 87 Experiment, Geophys. Res. Lett., 20, 1371–1374, 1993.

Lacerda, M., Couto, A., and Estanqueiro, A.: Wind Power Ramps Driven by Windstorms and Cyclones, Energies, 10, 1475, 2017.

Larsén, X. G. and Fischereit, J.: A case study of wind farm effects using two wake parameterizations in the Weather Research and Forecasting (WRF) model (V3.7.1) in the presence of low-level jets, Geosci. Model Dev., 14, 3141–3158, 2021.

690    Li, B., Basu, S., Watson, S. J., and Russchenberg, H. W. J.: Mesoscale modeling of a "Dunkelflaute" event, Wind Energy, 24, 5–23, 2021.

Li, J. and Chen, Y.-L.: Barrier jets during TAMEX, Monthly weather review, 126, 959–971, 1998.

Linden, S., Myers, B., and Haupt, S. E.: Observation-based wind-power ramp forecast system, in: Proc. American Meteorological Sciety Annual Meeting, pp. 22–26, 2012.

Mararakanye, N. and Bekker, B.: Renewable energy integration impacts within the context of generator type, penetration level and grid 695    characteristics, Renewable Sustainable Energy Rev., 108, 441–451, 2019.

Marjanovic, N., Wharton, S., and Chow, F. K.: Investigation of model parameters for high-resolution wind energy forecasting: Case studies over simple and complex terrain, J. Wind Eng. Ind. Aerodyn., 134, 10–24, 2014.

Mehta, M., Zaaijer, M., and von Terzi, D.: Drivers for optimum sizing of wind turbines for offshore wind farms, Wind Energy Science, 9, 141–163, 2024.

700    Mellor, G. L. and Yamada, T.: Development of a turbulence closure model for geophysical fluid problems, Reviews of Geophysics, 20, 851–875, 1982.

Mukul Tewari, N., Tewari, M., Chen, F., Wang, W., Dudhia, J., LeMone, M., Mitchell, K., Ek, M., Gayno, G., Wegiel, J., et al.: Implementation and verification of the unified NOAH land surface model in the WRF model (Formerly Paper Number 17.5), in: Proceedings of the 20th conference on weather analysis and forecasting/16th conference on numerical weather prediction, Seattle, WA, USA, vol. 14, 2004.

705    Nakanishi, M. and Niino, H.: An improved Mellor–Yamada level-3 model: Its numerical stability and application to a regional prediction of advection fog, Boundary-Layer Meteorology, 119, 397–407, 2006.

Nakanishi, M. and Niino, H.: Development of an improved turbulence closure model for the atmospheric boundary layer, Journal of the Meteorological Society of Japan. Ser. II, 87, 895–912, 2009.

National Centers for Environmental Prediction, National Weather Service, NOAA, U.S. Department of Commerce: NCEP GFS 0.25 Degree 710    Global Forecast Grids Historical Archive, https://doi.org/10.5065/D65D8PWK, 2015.

Nunalee, C. G. and Basu, S.: Mesoscale modeling of coastal low-level jets: implications for offshore wind resource estimation, Wind Energy, 17, 1199–1216, 2014.

Olauson, J.: ERA5: The new champion of wind power modelling?, Renewable energy, 126, 322–331, 2018.

Orlanski, I. and Ross, B.: The circulation associated with a cold front. Part I: Dry case, Journal of Atmospheric Sciences, 34, 1619–1633, 715    1977.

Parish, T. R. and Oolman, L. D.: On the role of sloping terrain in the forcing of the Great Plains low-level jet, Journal of the atmospheric sciences, 67, 2690–2699, 2010.

Pereyra-Castro, K. and Caetano, E.: Wind-Ramp Predictability, Atmosphere, 13, 453, 2022.

Pichault, M., Vincent, C., Skidmore, G., and Monty, J.: Characterisation of intra-hourly wind power ramps at the wind farm scale and
720    associated processes, Wind Energy Sci., 6, 131–147, 2021.

Ramon, J., Lledó, L., Torralba, V., Soret, A., and Doblas-Reyes, F. J.: What global reanalysis best represents near-surface winds?, Quarterly Journal of the Royal Meteorological Society, 145, 3236–3251, 2019.

Ridal, M., Bazile, E., Le Moigne, P., Randriamampianina, R., Schimanke, S., Andrae, U., Berggren, L., Brousseau, P., Dahlgren, P., Edvinsson, L., et al.: CERRA, the Copernicus European Regional Reanalysis system, Quarterly Journal of the Royal Meteorological Society,
725    2024.

Schimanke, S., Ridal, M., Le Moigne, P., Berggren, L., Undén, P., Randriamampianina, R., Andrea, U., Bazile, E., Bertelsen, T., Brousseau, P., Dahlgren, P., Edvinsson, L., El Said, A., Glinton, M., Hopsch, S., Isaksson, L., Mladek, R., Olsson, E., Verrelle, A., and Wang, Z.: CERRA sub-daily regional reanalysis data for Europe on pressure levels from 1984 to present, Tech. rep., Copernicus Climate Change Service (C3S) Climate Data Store (CDS), https://doi.org/10.24381/cds.a39ff99f, accessed on 10-10-2023, 2021.

730  Shin, H. H. and Hong, S.-Y.: Representation of the subgrid-scale turbulent transport in convective boundary layers at gray-zone resolutions, Monthly Weather Review, 143, 250–271, 2015.

Skamarock, W. C., Klemp, J. B., Dudhia, J., Gill, D. O., Liu, Z., Berner, J., Wang, W., Powers, J., Duda, M., Barker, D., et al.: A description of the advanced research WRF version 4, NCAR tech. note ncar/tn-556+ str, 145, 2019.

Smedman, A.-S., Tjernström, M., and Högström, U.: Analysis of the turbulence structure of a marine low-level jet, Boundary-layer meteo-
735    rology, 66, 105–126, 1993.

Smedman, A.-S., Bergström, H., and Högström, U.: Spectra, variances and length scales in a marine stable boundary layer dominated by a low level jet, Boundary-Layer Meteorology, 76, 211–232, 1995.

Smirnova, T., Kenyon, J., Turner, D., Brown, J., Zheng, W., and Green, B.: A description of the MYNN surface-layer scheme, NOAA Tech. Memo. OAR GSL-67, 2021.

740  Storm, B., Dudhia, J., Basu, S., Swift, A., and others: Evaluation of the weather research and forecasting model on forecasting low-level jets: Implications for wind energy, Wind Energy: An, 2009.

Tambke, J., Lange, M., Focken, U., Wolff, J.-O., and Bye, J. A.: Forecasting offshore wind speeds above the North Sea, Wind Energy: An International Journal for Progress and Applications in Wind Power Conversion Technology, 8, 3–16, 2005.

Tay, K., Koh, T.-Y., and Skote, M.: Characterizing mesoscale variability in low-level jet simulations for CBLAST-LOW 2001 campaign,
745    Meteorol. Atmos. Phys., 133, 163–179, 2021.

Thorpe, A. J. and Clough, S. A.: Mesoscale dynamics of cold fronts: Structures described by dropsoundings in FRONTS 87, Quarterly Journal of the Royal Meteorological Society, 117, 903–941, 1991.

Uccellini, L. W. and Johnson, D. R.: The coupling of upper and lower tropospheric jet streaks and implications for the development of severe convective storms, Monthly Weather Review, 107, 682–703, 1979.

750  Ueckerdt, F., Brecha, R., and Luderer, G.: Analyzing major challenges of wind and solar variability in power systems, Renewable Energy, 81, 1–10, 2015.

Valldecabres, L., Bremen, L., and Kühn, M.: Minute-scale detection and probabilistic prediction of offshore wind turbine power ramps using dual-Doppler radar, Wind Energy, 23, 2202–2224, 2020.

Vemuri, A., Buckingham, S., Munters, W., Helsen, J., and van Beeck, J.: Sensitivity analysis of mesoscale simulations to physics parame-
terizations over the Belgian North Sea using Weather Research and Forecasting – Advanced Research WRF (WRF-ARW), Wind Energy
Science, 7, 1869–1888, 2022.

Veron, D. E., Brodie, J. F., Shirazi, Y. A., and Gilchrist, J. R.: Modeling the electrical grid impact of wind ramp-up forecasting error offshore
in the Mid-Atlantic region, Journal of Renewable and Sustainable Energy, 10, 2018.

Wagner, D., Steinfeld, G., Witha, B., Wurps, H., and Reuder, J.: Low level jets over the southern North Sea, Meteorol. Z., 28, 389–415, 2019.

Wakimoto, R. M. and Murphey, H. V.: Airborne Doppler radar and sounding analysis of an oceanic cold front, Monthly weather review, 136,
1475–1491, 2008.

Wind Europe: Offshore wind in Europe: Key trends and statistics 2019, https://windeurope.org/about-wind/statistics/offshore/
european-offshore-wind-industry-key-trends-statistics-2019/, accessed on 18 October 2023, 2019.

Xing-Sheng, L., Gaynor, J., and Kaimal, J.: A study of multiple stable layers in the nocturnal lower atmosphere, Boundary-layer meteorology,
26, 157–168, 1983.

Zhao, J., Chen, X., and He, M.: Detection of impending ramp for improved wind farm power forecasting, in: 2019 IEEE Texas Power and
Energy Conference (TPEC), pp. 1–6, IEEE, 2019.

Zheng, C. W., Li, C. Y., Pan, J., Liu, M. Y., and Xia, L. L.: An overview of global ocean wind energy resource evaluations, Renewable and
Sustainable Energy Reviews, 53, 1240–1251, 2016.